Magnetic rotation and quasicollective structures in ^{58}Fe: Influence of the νg_{9/2} orbital

D. Steppenbeck, R. V. F. Janssens, S. J. Freeman, M. P. Carpenter, P. Chowdhury, A. N. Deacon, M. Honma, H. Jin, T. Lauritsen, C. J. Lister, J. Meng, J. Peng, D. Seweryniak, J. F. Smith, Y. Sun, S. L. Tabor, B. J. Varley, Y.-C. Yang, S. Q. Zhang, P. W. Zhao, and S. Zhu

Phys. Rev. C **85**, 044316 — Published 16 April 2012

DOI: 10.1103/PhysRevC.85.044316

Magnetic rotation and quasicollective structures in ^{58}Fe: Influence of the $\nu g_{9/2}$ orbital

D. Steppenbeck,[1,*] R. V. F. Janssens,[2] S. J. Freeman,[3] M. P. Carpenter,[2] P. Chowdhury,[4] A. N. Deacon,[3,†] M. Honma,[5] H. Jin,[6] T. Lauritsen,[2] C. J. Lister,[2] J. Meng,[7] J. Peng,[8] D. Seweryniak,[2] J. F. Smith,[3,‡] Y. Sun,[6,9,10] S. L. Tabor,[11] B. J. Varley,[3] Y.-C. Yang,[6] S. Q. Zhang,[7] P. W. Zhao,[7] and S. Zhu[2]

[1]*RIKEN Nishina Center, 2-1, Hirosawa, Wako, Saitama 351-0198, Japan*
[2]*Physics Division, Argonne National Laboratory, Argonne, Illinois 60439, USA*
[3]*Schuster Laboratory, University of Manchester, Manchester M13 9PL, United Kingdom*
[4]*Department of Physics, University of Massachusetts Lowell, Lowell, Massachusetts 01854, USA*
[5]*Center for Mathematical Sciences, Aizu University, Tsuruga, Ikki-Machi, Aizu-Wakamatsu, Fukushima 965-8580, Japan*
[6]*Department of Physics, Shanghai Jiao-Tong University, Shanghai 200240, People's Republic of China*
[7]*State Key Laboratory of Nuclear Physics and Technology, School of Physics, Peking University, Beijing 100871, People's Republic of China*
[8]*Department of Physics, Beijing Normal University, Beijing 100875, People's Republic of China*
[9]*Institute of Modern Physics, Chinese Academy of Sciences, Lanzhou 730000, People's Republic of China*
[10]*Department of Physics and Astronomy, University of Tennessee, Knoxville, Tennessee 37966, USA*
[11]*Department of Physics, Florida State University, Tallahassee, Florida 32306, USA*

The structure of ^{58}Fe was investigated at Gammasphere using ^{48}Ca(^{13,14}C,xn) fusion-evaporation reactions at a beam energy of 130 MeV. The level scheme has been revised and extended to $J \sim 17\hbar$ and an excitation energy of 16.6 MeV. Regular band structures consisting of low-energy $\Delta J = 1\hbar$ transitions have been observed at moderate spin ($J \sim 8 - 15\hbar$) and are candidates for magnetic rotational bands. Self-consistent tilted-axis-cranking calculations within a relativistic mean-field theory were applied to investigate these bands and were found to reproduce the experimental results well. In other parts of the level scheme, quasirotational bands composed of stretched-$E2$ transitions have been extended to high spin and other bands have been identified for the first time. Positive-parity experimental states were compared to predictions of the spherical shell model using the GXPF1A, KB3G, and FPD6 effective interactions in the fp model space. The projected shell model, with a deformed quasiparticle basis including the neutron $\nu g_{9/2}$ orbital, was applied to interpret regular $\Delta J = 2\hbar$ band structures that extend beyond the maximum spin available for $\pi[(f_{7/2})^{-2}] \otimes \nu[(p_{3/2}f_{5/2}p_{1/2})^4]$ configurations and exhibit features characteristic of rotational alignment. It is clear that the $\nu g_{9/2}$ intruder orbital plays an crucial role in describing the quasirotational structures in this nucleus, even starting as low as $J \sim 5\hbar$.

PACS numbers: 23.20.En, 23.20.Lv, 27.40.+z

I. INTRODUCTION

Over the past few decades, numerous experimental campaigns have been undertaken to study the changes in nuclear shell structure away from the stability line. In the case of the fp shell, which is bounded by $Z = 20-28$ and $N = 20-40$, recent studies have highlighted the onset of a significant subshell closure at $N = 32$ in the neutron-rich isotones ^{56}Cr [1–4], ^{54}Ti [5, 6], and ^{52}Ca [7, 8]. The onset of the new subshell gap has been attributed to the attractive proton-neutron (π-ν) interaction between the $\pi f_{7/2}$ and $\nu f_{5/2}$ single-particle orbitals [9]. As protons are removed from a full $\pi f_{7/2}$ orbital, the strength of the π-ν interaction decreases, causing the $\nu f_{5/2}$ orbital to shift up in energy relative to the $\nu p_{1/2}$ and $\nu p_{3/2}$ spin-orbit partners. At $Z = 24$, which corresponds to the $\pi f_{7/2}$ midshell, the $N = 32$ subshell closure begins to present itself via a rise in the energy of the first 2^+ state [$E(2_1^+)$], and a suppression of the $B(E2; 0_1^+ \rightarrow 2_1^+)$ reduced transition probability, relative to the neighboring even-even isotone ^{58}Fe and the isotopes ^{54}Cr and ^{58}Cr. The effect becomes even more pronounced for ^{54}Ti and ^{52}Ca, since the $\pi f_{7/2}$ orbital is effectively empty at $Z = 20$.

The onset of the $N = 32$ gap is reproduced well by the GXPF1 shell-model effective interaction [10] in the full fp model space. Another important manifestation of the GXPF1 Hamiltonian is the prediction of a significant subshell closure at $N = 34$ along the Ti and Ca isotopic chains; however, this was not verified by experiment in the case of ^{56}Ti [6, 11]. The interaction was modified as a result, leading to a new version, GXPF1A [12], by changing the strength of five $T = 1$ matrix elements mainly associated with the $\nu p_{1/2}$ orbital. The modified Hamiltonian was found to reproduce $E(2_1^+)$ for ^{56}Ti in a more satisfactory manner, and also resulted in system-

*Electronic address: steppenbeck@riken.jp
†Present address: Cargo Division, Rapsican Systems, Prospect Way, Victoria Business Park, Stoke-on-Trent ST8 7PL, United Kingdom
‡Present address: Department of Physics, University of the West of Scotland, Paisley PA1 2BE, United Kingdom

atic improvements in predictions of $E(2_1^+)$ along the Ti and Cr isotopic chains (see Fig. 1 of Ref. [12] for details). Despite these modifications, the more recent interaction still predicts a significant subshell closure at $N = 34$ for Ca isotopes. However, the experimental result for $E(2_1^+)$ in the case of ^{54}Ca, which is crucial for resolving significant differences between the predictions of GXPF1A and other fp-shell Hamiltonians, such as the KB3G [13] and FPD6 [14] interactions, is currently lacking.

Although the GXPF1A effective interaction accounts for experimental features in stable and moderately neutron-rich fp-shell nuclei rather well, its predictive power is found to breakdown at $N \approx 35$ for Cr and Fe. Various studies, for example Refs. [15, 16], have suggested that the influence of the $\nu g_{9/2}$ orbital becomes increasingly important in more exotic isotopes and that the fp model space alone is too restrictive. Other recent studies along the Cr [17, 18] and Fe [19] isotopic chains near $N = 40$ have further highlighted the impact of the $\nu g_{9/2}$ orbital and other states outside the fp shell that drive collectivity in these exotic systems. Attempts to extend the fp model space in shell-model calculations indicate the need to include the $\nu g_{9/2}$ and $\nu d_{5/2}$ orbitals to reproduce the low-lying levels in a more satisfactory manner [20]. In fact, this had already been recognized by some of the same authors [21] based on data from nuclei closer to stability.

Recently, the projected shell model (PSM) [22] has been applied to this mass region to investigate states in fp-shell systems to high spin. By exploiting the use of a deformed shell-model basis, the PSM can adopt a relatively large single-particle space that allows collective motion and cross-shell excitations to be taken into account. The PSM has successfully reproduced high-spin structural features in some fp-shell nuclei that involve $\nu g_{9/2}$ configurations (see, for example, Refs. [23–25]).

On the experimental side, the effect of the $\nu g_{9/2}$ orbital on the structures of neutron-rich nuclides has already been shown to induce deformation that leads to quasirotational bands at high spin in isotopes of Cr [16, 26], Mn [27, 28], and Fe [29, 30]. More specifically, in ^{55}Cr, a decoupled rotational band built on a $J = 9/2\hbar$ state at 2087 keV was deduced to be one of positive parity [2]. These results indicate that a parity change occurs relative to the low-lying states, which suggests that the configuration of the band involves at least one neutron in the $\nu g_{9/2}$ orbital. More recently, this band was extended to $J^\pi = 33/2^+$ [31], the terminating spin expected from the $\pi[(f_{7/2})^4] \otimes \nu[(p_{3/2}f_{5/2}p_{1/2})^2(g_{9/2})^1]$ configuration, which confirms the conclusion drawn in Ref. [2].

Thus, with the experimental evidence already at hand, it is clear that the $\nu g_{9/2}$ orbital plays a pivotal role in describing the structures of exotic fp nuclei. In fact, even in cases closer to stability, the $\nu g_{9/2}$ state might be naïvely expected to have an influence at intermediate to high spin. In the present study, the yrast structure of ^{58}Fe has been investigated to $J \sim 17\hbar$ to address this issue further.

In addition to the studies discussed above, the experimental discovery of regular, rotational-like bands of $\Delta J = 1\hbar$ transitions in near-spherical Pb isotopes and other groups of nuclei has opened a new era in high-spin physics over the last 20 years or so (see, for example, Refs. [32–34]). Unlike traditional deformed rotational bands, these structures are composed of strong $M1$ and weak $E2$ transitions. The orientation of these rotors is not specified by the deformation of the overall matter density, but rather by the current distribution induced by specific nucleons moving in high-j orbitals.

The explanation of such bands in terms of the "shears mechanism" was first proposed in Ref. [35], where the generation of $M1$ sequences was explained and a decrease in $B(M1)$ strength with spin was predicted. In this interpretation, the angular momentum vectors of high-j protons and neutrons form two blades of a pair of shears that are almost perpendicular to each other at the bandhead. Up the band, energy and angular momentum are increased by closing the blades of the shears, i.e., by aligning the proton and neutron angular momenta. Consequently, rotational bands can be formed in spite of the fact that the shapes of these nuclei stay nearly spherical. In order to distinguish this kind of rotation from the usual collective rotation in well-deformed nuclei, the name "magnetic rotation" [36] was introduced, which alludes to the fact that the magnetic moment is the order parameter inducing a violation of rotational symmetry and, therefore, causing the presence of rotational-like structures in the spectrum.

On the experimental side, long cascades of magnetic dipole transitions were first observed in neutron-deficient isotopes of Pb [37–39]. Later, lifetime measurements by Clark *et al.* [40] for four $M1$ bands in ^{198,199}Pb provided clear evidence for magnetic rotation. Numerous magnetic rotational bands have since been observed not only in the mass region $A \sim 190$, but also at $A \sim 140$, ~ 110, and ~ 80. More than 130 magnetic dipole bands have now been identified in these four mass regions [41]. The presence of magnetic rotational bands in the fp shell, however, is extremely scarce. To date, only one experimental case has been reported for ^{60}Ni [42], where four candidate bands were identified.

On the theoretical side, the tilted-axis-cranking (TAC) model [35] has been widely used to describe magnetic rotation because, in this framework, it is easy to construct classical vector diagrams showing the angular momentum composition. After the first self-consistent TAC solutions were found [35], the characteristics of the TAC approximation were discussed and tested with the particle-rotor model [43]. Because of the high numerical complexity of the TAC model, most of the applications are based on simple schematic Hamiltonians, such as the pairing-plus-quadrupole model [35], while fully self-consistent calculations based on universal density functionals are relatively rare. Only recently, relativistic [44, 45] and nonrelativistic [46, 47] density functionals were used for fully microscopic investigations of magnetic rotation and chi-

rality.

The covariant density functional theory has received wide attention during the past two decades due to its success in describing many nuclear phenomena in stable as well as exotic nuclei [48, 49]. On the basis of the same functionals, and without any additional parameters, rotational excitations can be described in practical applications within the self-consistent, cranked relativistic mean-field (RMF) framework. The cranked RMF equations with arbitrary orientation of the rotational axis, i.e., three-dimensional cranking, have been developed in Ref. [44]. However, due to its numerical complexity, it has only been applied so far to the investigation of magnetic rotation in ^{84}Rb. Focusing on the magnetic rotational bands, a new computer code for the self-consistent, two-dimensional cranking RMF theory was established [45], which includes significant improvements. Very recently, the TAC model based on relativistic point-coupling Lagrangians was established and applied to magnetic rotation in ^{60}Ni [50] and ^{198,199}Pb [51]. Moreover, with the same effective interaction PC-PK1 [52] for the same Lagrangian, the first microscopic description of "antimagnetic rotation" has been given for ^{105}Cd [53].

In the present work, the self-consistent TAC-RMF model based on a point-coupling interaction has been applied to investigate magnetic rotational band candidates in ^{58}Fe. In other parts of this paper, the experimental procedures are outlined and a new level scheme is presented (Sections II and III, respectively). A discussion of the results is provided in Section IV.

II. EXPERIMENTS

Data were obtained from two independent experiments using 130-MeV ^{48}Ca beams on thin ^{13,14}C targets (~ 100 μg/cm^2) to investigate fusion-evaporation reaction products with the Gammasphere array [54]. The ^{48}Ca beam was delivered by the Argonne Tandem Linear Accelerator System (ATLAS) [55, 56]. Results from the same experiments are reported elsewhere for $^{56-60}$Cr [16, 26], $^{57-60}$Mn [27], and ^{59,60}Fe [29], where further details of the experimental procedures and data analysis techniques are also documented.

In the present study, Gammasphere was used in standalone mode to measure γ-ray coincidences of multiplicity three and four, or higher, without particle identification, over time periods of 12 and 19 h for the ^{13,14}C target experiments, respectively. These high-fold events were sorted into γ^3 coincidence cubes and subsequently analyzed using standard γ-ray coincidence techniques. New transitions in ^{58}Fe were identified on the basis of coincidence relationships with known γ rays, which are compiled in Refs. [57, 58]. Transition intensities were measured using data from the ^{13}C target experiment, since a larger number of γ rays were identified in that reaction.

The spins and parities of excited states were investigated, where possible, using γ-ray angular distributions [59, 60] and directional correlations of oriented (DCO) states [61].

Angular distributions were obtained from nine rings of Gammasphere detectors ranging from $\theta = 90^\circ$ to 163°, where $\theta = 0^\circ$ defines the downstream direction of the beam line. The detectors at forward angles ($\theta < 90^\circ$) were omitted due to the presence of strong neutron-induced peaks in the γ-ray spectra. Raw γ-ray intensities were corrected for differences in the relative efficiencies of the detector rings using a standard ^{152}Eu calibration source. Angular distributions, $W(\theta)$, were fitted [59, 60] to

$$W(\theta) = A_0[1 + a_2 P_2(\cos\theta) + a_4 P_4(\cos\theta)], \qquad (1)$$

where $P_{2,4}(\cos\theta)$ are Legendre polynomials and $a_{2,4}$ are the normalized angular distribution coefficients.

In cases where the transition intensity was too low to make measurements at each ring angle, three rings near 90° (specifically, $\theta = 90^\circ$, 99°, and 101°) were summed together to form one spectrum, and similarly, another spectrum was obtained for the three rings closest to 180° ($\theta = 143^\circ$, 148°, and 163°). The ratio of the γ-ray intensities (I_γ) from these two spectra, $R_{180/90}$, given by

$$R_{180/90} = \frac{\sum_{\theta=143^\circ}^{163^\circ} I_\gamma^\theta}{\sum_{\theta=90^\circ}^{101^\circ} I_\gamma^\theta}, \qquad (2)$$

was used to deduce the character of the γ ray by assuming that $R_{180/90} < 1$ for stretched-dipole transitions, and $R_{180/90} > 1$ for stretched-quadrupole transitions. Mixed transitions are exceptions to these general rules, and care must be taken when proposing spin-parity (J^π) assignments in these cases; several situations were encountered in the present study, which are discussed in more detail in Section III.

The same two subsets of detector rings were adopted for the DCO method as those used for $R_{180/90}$. DCO ratios, $R_{\rm DCO}$, were deduced [61] using

$$R_{\rm DCO} = \frac{I_{\gamma_2}^{\theta_1}(\mathrm{Gate}_{\gamma_1}^{\theta_2})}{I_{\gamma_2}^{\theta_2}(\mathrm{Gate}_{\gamma_1}^{\theta_1})}, \qquad (3)$$

where $I_{\gamma_2}^{\theta_1}(\mathrm{Gate}_{\gamma_1}^{\theta_2})$ represents the intensity of transition γ_2 in detectors at the angle θ_1 when an energy gate is set on transition γ_1 at θ_2, and similarly for $I_{\gamma_2}^{\theta_2}(\mathrm{Gate}_{\gamma_1}^{\theta_1})$. Here, the angles θ_1 and θ_2 represent either the group of detectors at $\sim 90^\circ$ or $\sim 180^\circ$, rather than one discrete value. Typical values deduced in the present study were $R_{\rm DCO} \sim 1.0$ and $\gtrsim 1.6$ for stretched-dipole and stretched-quadrupole transitions, respectively, when the energy gate was set on a dipole transition. When the energy gate was placed on a stretched-quadrupole transition, the respective typical values were $R_{\rm DCO} \lesssim 0.6$ and ~ 1.0 for stretched dipoles and quadrupoles. These limits were used for assignments of $\Delta J = 1$ or $2\hbar$, where possible.

III. LEVEL SCHEME

The ^{58}Fe level scheme deduced in the present study is given in Figs. 1 and 2, with specific details of the energy levels and γ-ray transitions listed in Table I.

A previous high-spin study of ^{58}Fe was reported by Nathan *et al.* [62], where excited states were populated to $J \sim 13\hbar$ at 10 MeV, corresponding to the 10072-keV level in Fig. 2. The placement of all transitions identified in Ref. [62], with the exception of the ordering of the 264- and 1805-keV γ rays, are confirmed by the present study.

The most recent data reported for ^{58}Fe prior to the present work come from a ^{48}Ca(^{13}C,3n) fusion-evaporation reaction by Appelbe *et al.*, using an array of 20 high-purity Ge detectors. However, those results are only available as a private communication to Refs. [57, 58], and many tentative transitions are included in these compilations. Despite the uncertainties, the level scheme was extended to $J \sim 15\hbar$ at 12.8 MeV by Appelbe *et al.* [57, 58], which corresponds to the 12815-keV level in Fig. 2, and ten other states at lower energy were identified for the first time. Many, but not all of the new transitions and energy levels have been confirmed by the present study.

In the level scheme reported here (see Figs. 1 and 2), the high-spin structure has been extended further, to $J \sim 17\hbar$ at around 16.6 MeV, with the addition of several non-yrast bands as well. The spin-parity assignments can be deduced from the $a_{2,4}$ coefficients, $R_{180/90}$ values, and DCO ratios given in Table I. However, for the sake of clarity and completeness, the proposed assignments will be addressed throughout the discussion of the level scheme. Also, some of the J^π assignments require an explanation due to the presence of mixed transitions.

TABLE I: Energy levels and γ-ray transitions deduced in the present work. All energies are given in keV and intensities are normalized to 100. The columns labeled DCO$^{(d)}$ and DCO$^{(q)}$ refer to energy gates set on the 783-keV, stretched-dipole and 1266-keV, stretched-quadrupole transitions, respectively. The final two columns are intended to aid the identification of γ rays in Figs. 1 and 2; B1–B5 are used as a shorthand notation for Bands 1–5, respectively.

$E_{\rm level}$	J^π	E_γ	I_γ	a_2	a_4	$R_{180/90}$	DCO$^{(d)}$	DCO$^{(q)}$	ΔJ	Figure	Placement
810.6(3)	2^+	810.8(3)	100(5)	0.16(1)	-0.06(1)	1.18(1)	1.47(1)	0.90(1)	2	1	GSB
1674.7(3)	2^+	864.1(2)	$\geq$5.7(3)						0	1	γVB$\rightarrow$GSB
		1674.4(5)	$\geq$4.6(3)						2	1	γVB$\rightarrow$GSB
2076.7(3)	4^+	1265.9(3)	75(3)	0.31(1)	-0.13(1)	1.41(2)	1.71(1)		2	1	GSB
2133.9(3)	3^+	459.0(3)	4.0(1)	-0.33(1)		0.68(2)			1	1	γVB
		1323.4(3)	13.5(4)	-0.19(2)	0.04(2)	0.86(2)			1	1	γVB$\rightarrow$GSB
2600.5(3)	4^+	466.3(3)	3.8(1)	-0.43(2)		0.60(2)			1	1	γVB
		523.7(3)	13.2(4)	0.20(1)	-0.09(1)	1.26(2)		1.02(2)	0	1	γVB$\rightarrow$GSB
		925.9(3)	6.3(2)	0.31(4)[a]	-0.20(7)[a]				2	1	γVB
		1790.0(5)	14.1(4)	0.26(4)	-0.23(6)	1.44(17)			2	1	γVB$\rightarrow$GSB
3449.9(4)	5^+	849.1(4)	3.4(1)	-0.56(7)[a]					1	1	γVB
		1316.1(3)	4.5(1)	0.35(3)	-0.09(4)	1.61(8)			2	1	γVB
3597.3(4)	6^+	147.5(10)	0.035(2)						1	1	GSB$\rightarrow\gamma$VB
		1520.8(4)	39.4(12)	0.30(1)	-0.09(1)	1.44(2)	1.70(3)	1.02(1)	2	1	GSB
3886.8(4)	6^+	289.4(5)	11.0(3)	0.34(1)	-0.07(1)	1.46(1)	1.80(2)	1.07(1)	0	1	K=6$\rightarrow$GSB
		436.8(4)	0.23(1)			0.72(12)	0.74(15)		1	1	K=6$\rightarrow\gamma$VB
		1286.2(3)	2.2(1)	0.47(4)	-0.24(6)	1.56(25)	2.16(25)		2	1	K=6$\rightarrow\gamma$VB
		1810.1(6)	31.2(9)	0.32(1)*	-0.13(2)*	1.48(5)*	1.73(2)	1.04(1)*	2	1	K=6$\rightarrow$GSB
4215.0(4)	5	764.6(6)	0.43(1)			0.91(6)†		0.74(4)†	0	2	B2$\rightarrow\gamma$VB
		1614.6(4)	10.3(3)	-0.17(3)[a]					1	2	B2$\rightarrow\gamma$VB
		2138.1(10)	3.0(1)						1	2	B2$\rightarrow$GSB
4405.5(4)	6^+	518.5(4)	0.68(2)						0	1	γVB$\rightarrow K$=6
		955.8(3)	1.16(4)			0.91(7)**			1	1	γVB
		1805.3(6)	4.3(1)	0.32(1)*	-0.13(2)*	1.48(5)*		1.04(1)*	2	1	γVB
		2330.0(17)	2.4(1)						2	1	γVB$\rightarrow$GSB
4669.9(4)	7	264.4(6)	2.5(1)	-0.19(1)	-0.09(1)	0.78(2)		0.58(2)	1	2	B2$\rightarrow\gamma$VB
		454.6(4)	6.8(2)	0.39(3)	-0.04(4)	1.62(13)		1.17(8)	2	2	B2
		783.0(3)	21.8(7)	-0.20(1)	-0.02(1)	0.81(2)		0.58(1)	1	2	B2$\rightarrow K$=6
		1072.6(3)	12.1(4)					0.58(1)	1	2	B2$\rightarrow$GSB
5086.7(4)	6	416.5(4)	0.10(1)						1	2	B3$\rightarrow$B2
		871.7(3)	0.72(2)						1	2	B3$\rightarrow$B2
		1637.2(5)	2.4(1)						1	2	B3$\rightarrow\gamma$VB
5344.3(4)	8^+	1457.2(4)	10.7(3)	0.29(1)	-0.08(2)	1.45(3)		1.05(3)	2	1	B1$\rightarrow K$=6
		1747.1(5)	3.7(1)	0.15(7)§	-0.12(8)§	1.30(23)§		1.10(6)§	2	1	B1$\rightarrow$GSB

TABLE I. *(Continued.)*

$E_{\rm level}$	J^π	E_γ	I_γ	a_2	a_4	$R_{180/90}$	DCO$^{\rm (d)}$	DCO$^{\rm (q)}$	ΔJ	Figure	Placement
5503.5(4)	8^+	1906.9(8)	8.8(3)	0.35(1)‡	-0.16(1)‡	1.55(1)‡		1.10(4)‡	2	1	GSB
5832.7(4)	9	329.0(4)	0.079(4)						1	2	B2→GSB
		1162.8(3)	29.5(9)	0.27(1)	-0.20(1)	1.48(2)	1.88(2)	1.10(1)	2	2	B2
5833.2(5)	(7)	1947.4(13)	0.48(2)						(1)	2	B5→K=6
		2235.9(9)	2.7(1)						(1)	2	B5→GSB
6033.8(4)	8	201.3(8)	0.062(3)						1	2	B3→B2
		947.1(3)	1.9(1)	0.39(4)^a					2	2	B3
		1363.9(3)	5.0(2)	0.69(3)	0.12(4)	2.08(19)	2.41(12)	1.49(6)	1	2	B3→B2
6105.7(5)	8^+	601.7(4)	0.78(3)						0	1	K=6→GSB
		2220.3(13)	1.22(4)						2	1	K=6 band
		2508.7(14)	1.7(1)					1.17(15)	2	1	K=6→GSB
6283.7(4)	$9^{(+)}$	780.7(5)	0.84(3)						1	1	B1→GSB
		939.2(3)	8.8(3)					0.74(3)	1	1	B1
7169.7(5)	(9)	1063.3(7)	0.58(2)						(1)	2	B5→K=6
		1136.0(6)	0.16(1)						(1)	2	B5→B3
		1336.5(4)	1.34(4)						(2)	2	B5
		1336.8(6)	1.10(3)						(0)	2	B5→B2
		1666.2(6)	1.9(1)						(1)	2	B5→GSB
7243.4(5)	$10^{(+)}$	959.8(3)	4.6(1)			0.91(7)**		0.71(7)	1	1	B1
		1739.8(7)	0.77(3)						2	1	B1→GSB
7251.6(5)	9	1145.8(3)	0.40(2)						1	1	Into K=6
		1748.3(10)	0.71(3)	0.15(7)§	-0.12(8)§	1.30(23)§		1.10(6)§	1	1	Into GSB
7457.0(5)	10	1423.1(3)	4.8(2)						2	2	B3
		1624.3(5)	3.1(1)	0.31(6)^a			1.59(9)		1	2	B3→B2
7524.2(7)	(8)	2021.7(9)¶	0.17(1)						(0)	2	MRB2→GSB
		3926(7)	0.33(2)						(2)	2	MRB2→GSB
7657.8(8)	(8)	2988(4)	0.27(2)						(1)	2	MRB1→B2
7730.8(5)	11	1897.7(6)	16.1(5)	0.35(1)‡	-0.16(1)‡	1.55(1)‡	1.94(3)	1.10(4)‡	2	2	B2
7915.7(5)	(9)	392.1(7)	0.018(2)						(1)	2	MRB2
		1632.0(6)	1.37(4)						(0)	2	MRB2→B1
		2082.7(15)¶	0.23(1)						(0)	2	MRB2→B2
		2571.2(15)	0.22(1)						(1)	2	MRB2→B1
7942.0(5)	10^+	690.5(5)	0.19(1)						1	1	Out of GSB
		1836.3(10)	0.20(1)						2	1	GSB→K=6
		2439.9(12)	1.5(1)					1.21(15)	2	1	GSB
7965.3(6)	(10, 11)	2133.0(11)	0.94(3)						(1,2)	2	Into B2
8041.9(5)	(9)	384.1(7)	0.037(2)						(1)	2	MRB1
		2007.5(8)	0.64(2)						(1)	2	MRB1→B3
		2208.6(8)	2.0(1)				1.70(26)		(0)	2	MRB1→B2
		2538.8(23)	0.38(1)						(1)	2	MRB1→GSB
8171.9(5)	(9, 10)	230.6(6)¶	0.015(2)						(1,0)	2	Into GSB
		1001.5(9)	0.35(1)						(0,1)	2	Into B5
		1887.5(19)¶	0.38(1)						(0,1)	2	Into B1
		2338.1(15)	0.84(3)						(0,1)	2	Into B2
		2667.3(18)	0.41(2)						(1,2)	2	Into GSB
8424.1(7)	(10^+)	1171.6(12)	0.20(1)						(1)	2	Out of B4
		2321(3)	0.23(1)						(2)	2	B4→K=6
		2592.2(18)	0.57(2)						(1)	2	B4→B2
		2920.4(23)	0.73(3)						(2)	2	B4→GSB
8428.9(5)	(10)	513.3(4)	0.81(3)						(1)	2	MRB2
		697.9(4)	0.084(4)						(1)	2	MRB2→B2
		1185.1(11)	0.14(1)						(0)	2	MRB2→B1
		2145.0(9)	0.80(3)						(1)	2	MRB2→B1
		2596.6(13)	0.56(2)						(1)	2	MRB2→B2
8520.6(9)	(10^+)	2688.7(19)	0.50(2)						(1)	2	Into B2
		3019.3(22)	0.51(2)						(2)	2	Into GSB
8540.2(5)	(10)	368.4(4)	0.25(1)						(1,0)	2	Out of MRB1
		498.1(4)	1.5(1)			0.80(7)		0.61(5)	(1)	2	MRB1
		1083.1(6)	0.37(1)						(0)	2	MRB1→B3
		2256.6(9)	0.81(3)						(1)	2	MRB1→B1
		2707.5(14)	1.34(4)					0.92(12)	(1)	2	MRB1→B2

TABLE I. *(Continued.)*

$E_{\rm level}$	J^π	E_γ	I_γ	a_2	a_4	$R_{180/90}$	DCO$^{\rm (d)}$	DCO$^{\rm (q)}$	ΔJ	Figure	Placement
8747.9(14)	(10^+)	1496.5(13)	0.26(1)						(1)	1	Out of K=6
		2640(4)¶	0.15(1)						(2)	1	K=6 band
8888.9(6)	(11^+)	1645.5(6)	1.6(1)						(1)	1	B1
		2605.8(23)	0.12(1)						(2)	1	B1
8928.8(5)	(11)	388.6(5)¶	0.005(3)						(1)	2	B5→MRB1
		985.9(9)	0.15(1)						(1)	2	B5→GSB
		1198.0(4)	0.42(2)						(0)	2	B5→B2
		1759.2(5)	2.1(1)					1.19(24)	(2)	2	B5
		3100(3)¶	0.72(3)						(2)	2	B5→B2
9163.6(5)	(11)	623.3(3)	2.4(1)						(1)	2	MRB1
		1198.5(6)	0.23(1)						(1,0)	2	Out of MRB1
		1432.4(11)	0.30(1)						(0)	2	MRB1→B2
		1706.3(19)	0.26(1)						(1)	2	MRB1→B3
		1920.7(9)	0.34(1)						(1)	2	MRB1→B1
		1993.5(14)	0.49(2)						(2)	2	MRB1→B5
9174.6(5)	(11)	745.6(4)	1.43(4)						(1)	2	MRB2
		1931.5(8)	0.39(1)						(1)	2	MRB2→B1
		3346.9(23)	0.29(1)						(2)	2	MRB2→B2
9444.6(7)	12	1714.1(10)	0.55(2)						1	2	B3→B2
		1987.5(7)	3.5(1)	0.40(2)	-0.28(3)	1.64(9)	1.95(12)	1.06(5)	2	2	B3
9697.5(9)	(11)	1754.4(21)	0.05(1)						(1)	1	Into GSB
		2453.3(12)	0.54(2)						(1)	1	Into B1
9924.7(5)	(12)	749.9(7)	0.034(2)						(1)	2	MRB1→MRB2
		761.2(3)	1.8(1)			0.91(6)†		0.74(4)†	(1)	2	MRB1
		1959.4(8)	0.23(1)						(2,1)	2	Out of MRB1
		2192.6(14)	0.44(1)						(1)	2	MRB1→B2
9983.0(6)	$12^{(+)}$	1094.1(4)	0.080(4)						(1)	2	B4→B1
		1462.9(8)	0.35(1)						(2)	2	Out of B4
		1558.9(6)	0.60(2)						(2)	2	B4
		2041.0(22)	0.18(1)						2	2	B4→GSB
		2252.2(9)	2.2(1)					0.68(6)	1	2	B4→B2
		2740.8(15)	0.07(1)						2	2	B4→B1
9994(4)¶		3709(5)¶	0.19(1)							1	Into B1
10063(5)		3780(5)	0.22(1)							1	Into B1
10072.1(6)	13	2341.3(8)	4.3(1)	0.34(3)	-0.09(4)	1.56(6)	2.12(9)	1.16(8)	2	2	B2
10089.8(7)	(12^+)	1200.9(4)	0.58(2)						(1)	1	B1
		2846.5(23)	0.15(1)						(2)	1	B1
10095.7(6)	(12)	921.1(4)	0.66(2)						(1)	2	Into MRB2
		2364.1(14)	0.90(3)						(1)	2	Into B2
10130.5(5)	(12)	956.0(4)	0.67(2)						(1)	2	MRB2
		966.8(3)	0.67(2)						(1)	2	MRB2→MRB1
		1201.5(9)	0.32(1)						(1)	2	MRB2→B5
		2165.0(9)¶	0.22(1)						(2,1)	2	Out of MRB2
10152(3)		2909(3)	0.09(1)							1	Into B1
10352.7(10)	13	2622.5(15)	0.80(3)				2.09(46)	1.21(21)	2	2	Into B2
10685(3)	(13)	2954(3)	0.46(2)						(2)	2	Into B2
10918.2(14)		3675.5(23)	0.29(1)							1	Into B1
10952.4(5)	(13)	821.8(4)	0.85(3)						(1)	2	MRB1→MRB2
		1027.6(3)	1.44(4)						(1)	2	MRB1
		1511.1(23)	0.40(1)						(1)	2	MRB1→B3
		3223(4)	0.42(1)						(2)	2	MRB1→B2
10994.7(24)		3263.9(24)	0.23(1)							2	Into B2
11051.0(10)	(12^+)	1353.5(8)	0.06(1)						(1)	1	Out of GSB
		2161.9(16)	0.09(1)						(1)	1	GSB→B1
		3110(3)	0.09(1)						(2)	1	GSB
11168.7(16)		1470.9(15)	0.08(1)							1	
		3229(4)¶	0.02(1)							1	Into GSB
11209.3(16)	(13)	2280.6(15)	0.44(2)			1.56(13)		1.13(31)	(2)	2	B5
11652(6)¶		3710(6)¶	0.03(1)							1	Into GSB
11826(5)		3884(4)	0.06(1)							1	Into GSB
11852.7(6)	(14)	900.1(4)	0.33(1)						(1)	2	B3→MRB1

TABLE I. *(Continued.)*

$E_{\rm level}$	J^π	E_γ	I_γ	a_2	a_4	$R_{180/90}$	DCO$^{\rm (d)}$	DCO$^{\rm (q)}$	ΔJ	Figure	Placement
		1780.9(14)	0.38(1)						(1)	2	B3→B2
		2408.4(16)	0.89(3)						(2)	2	B3
11878(4)		1884.4(10)¶	0.05(5)							1	
		4636(7)	0.04(1)							1	Into B1
11906.6(8)	$14^{(+)}$	1833.5(9)	0.26(1)						1	2	B4→B2
		1924.2(7)	1.34(4)				1.83(37)		2	2	B4
11915.3(11)		997.4(13)¶	0.023(2)							1	
		2216.7(12)	0.14(1)							1	
		3028.2(18)¶	0.030(3)							1	Into B1
12017.0(6)	(14)	1064.6(4)	1.7(1)						(1)	2	MRB1
		1664.6(10)	0.46(2)						(1)	2	Out of MRB1
		1944.8(8)	0.31(1)						(1)	2	MRB1→B2
12047.4(17)		1694.7(14)	0.20(1)							2	
12176.3(7)	(14)	1223.8(8)	0.17(1)						(1)	2	Into MRB1
		2104.5(8)	0.35(1)						(1)	2	Into B2
		2731.0(12)	0.20(1)						(2)	2	Into B3
12215(5)		2151.3(18)	0.01(1)							1	
12346(3)¶		2194.1(15)¶	0.004(4)							1	
12470.0(21)		1551.6(17)	0.017(4)							1	Out of B1
		3584(6)	0.032(4)							1	B1
12532.8(9)		2460.9(9)	0.18(1)							2	Into B2
		2549.2(14)¶	0.01(1)							2	Into B4
		2609(3)	0.06(1)							2	Into MRB1
12814.9(10)	15	2743.7(12)	0.64(2)				1.75(44)		2	2	B2
12829(5)		3940(5)	0.037(4)							1	Into B1
12952.2(15)		1036.9(9)	0.10(1)							1	
13032(3)		2942(3)	0.006(3)							1	B1
13109(3)		3037(3)	0.05(1)							2	Into B2
13173.4(8)	(15)	1156.7(8)	1.03(3)						(1)	2	MRB1
		1320.4(7)	0.18(1)						(1)	2	MRB1→B3
13232.8(22)		2314.6(17)	0.028(4)							1	
13612(4)		3523(4)	0.021(3)							1	Into B1
13769(3)	(15)	2559.6(21)	0.05(1)						(2)	2	B5
13904(3)		3831.9(25)	0.11(1)							2	Into B2
13963(4)		3874(3)	0.012(3)							1	Into B1
14173.1(17)		1220.9(9)	0.017(3)							1	
14265.0(10)	(16)	1450.4(8)	0.08(1)						(1)	2	B3→B2
		2246.6(16)	0.14(1)						(2)	2	B3→MRB1
		2412.0(13)	0.09(1)						(2)	2	B3
14314.5(15)	(16^+)	2407.9(13)	0.42(2)						(2)	2	B4
16281(4)	(17)	3466(4)	0.020(4)						(2)	2	B2
16484(6)		3669(6)	0.018(4)							2	Into B2
16607(4)¶		3792(4)¶	0.027(4)							2	Into B2

[a]Coefficients ($a_{2,4}$) deduced from < 9 data points

*,**,†,‡,§Values for unresolved doublets

¶Placement in level scheme tentative

The ground-state band, Band 1, and other positive-parity states. The ground-state band (GSB) in Fig. 1 forms a regular sequence of stretched-$E2$ transitions from the 0^+ ground state to $J^\pi = 10^+$ at 7942 keV. This band has been tentatively extended to $J^\pi = 12^+$ at 11051 keV by assuming that the 3110-keV γ ray, which is coincident with the lower members of the GSB, continues the series of quadrupole transitions at lower energy. Angular distributions for the 1266- and 1907-keV transitions are presented in Figs. 3(d) and 3(f), respectively, as examples of typical plots for $\Delta J = 2\hbar$ γ rays in the band. Despite the fact that the 1907-keV peak forms an unresolved doublet with the 1898-keV line in Band 2 of comparable intensity (discussed later), the summed angular distribution is characteristic of a stretched-quadrupole transition. Therefore, both γ rays are assumed to be of $E2$ character here, in agreement with previous studies [57, 58]. Figure 4(a) provides a spectrum formed by placing two simultaneous energy gates (hereafter referred to as double gates) at 1266 and 1521 keV. The spectrum reveals the quality of the data available in the present study and provides evidence for the placement of some of the transitions in the GSB and other parts of the level scheme.

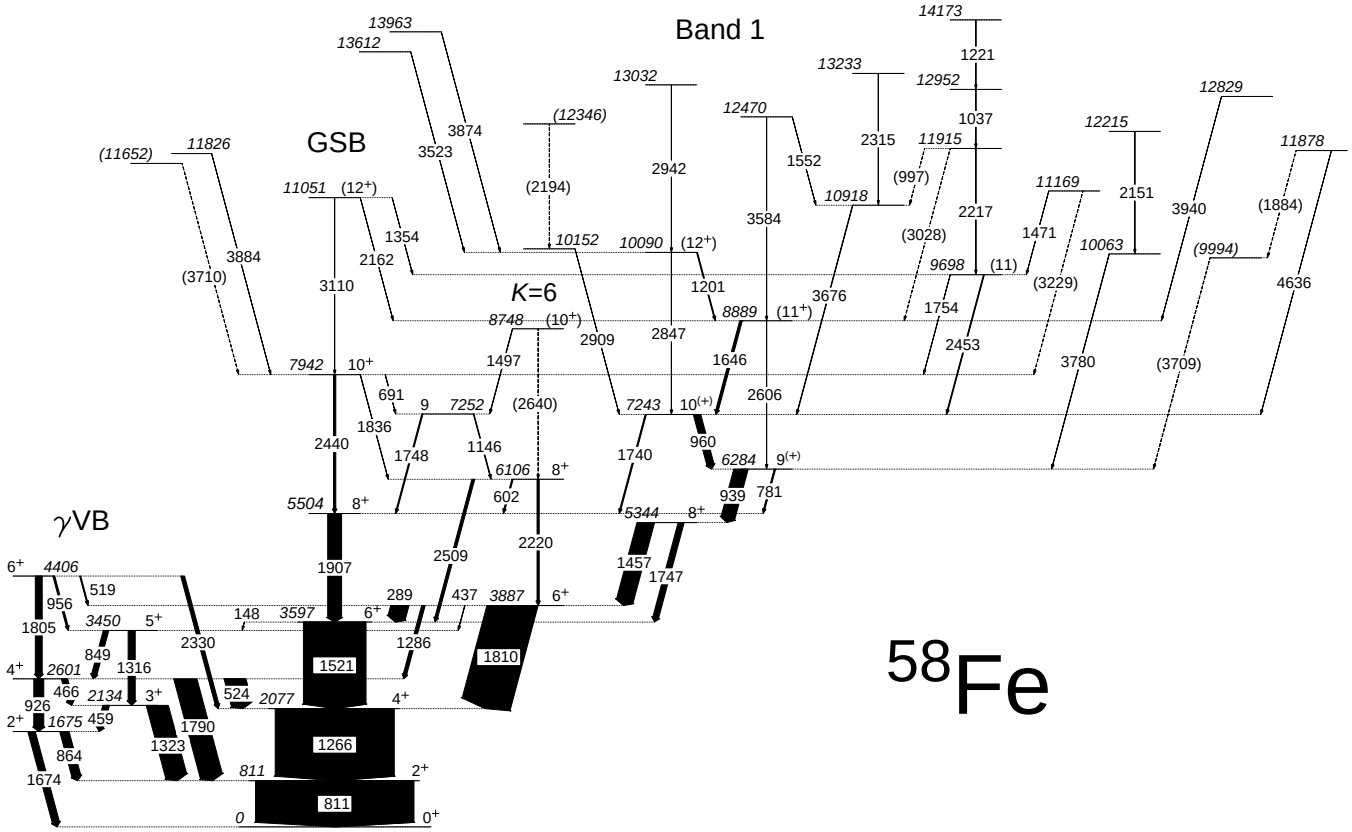

FIG. 1: Partial level scheme for ^{58}Fe deduced in the present study. Arrow widths are proportional to γ-ray intensities and tentative transitions are indicated by dashed lines and parentheses. Other parts of the level scheme are presented in Fig. 2.

To the left of the GSB in Fig. 1 is a positive-parity structure that begins with a 2^+ state at 1675 keV and extends in steps of $\Delta J = 1\hbar$ up to a 6^+ level at 4406 keV. Some of the levels are also connected by stretched-$E2$ transitions, and the structure displays the characteristics of a coupled band. It is noted that the level at 4406 keV results from a reordering of the 264- (see Fig. 2) and 1805-keV transitions relative to previous studies [57, 58], which reported a level at 2865 keV. The identification of the 519-, 956-, and 2330-keV γ rays here confirms the placement of the state at 4406 keV, and the spin-parity quantum numbers of all the levels in the structure are given unambiguously. This structure was previously described as a γ-vibrational band (γVB) in Ref. [63], which reported $J^\pi = 2^+$, 3^+, 4^+, and 5^+ states at 1675, 2134, 2600, and 3449 keV, respectively. Thus, this band has now been extended to include a $J^\pi = 6^+$ candidate state at 4406 keV, and the previously tentative spin-parity quantum numbers of the 5^+ state have been confirmed.

On the right-hand side of the GSB are several other positive-parity states, including the structure labeled Band 1 in Fig. 1. The unambiguous assignments of $J^\pi = 6^+$, 8^+, and 8^+ to the levels at 3887, 5344, and 6106 keV, are the result of the quadrupole nature of the 1286- and 1810-keV, the 1457- and 1747-keV, and the 2220- and 2509-keV transitions, respectively. The $R_{180/90}$ value for the weak 437-keV γ ray (see Table I) is consistent with other stretched-dipole transitions, and confirms the spin assignment for the level at 3887 keV. The angular distribution for the 289-keV γ ray, presented in Fig. 3(a), appears to be very similar to those for the stretched-quadrupole transitions. However, the mixing ratio for the 289-keV line was deduced to be $\delta \sim -0.7$, and, therefore, the γ ray is placed in the level scheme as a $\Delta J = 0$ transition of mixed character.

The structure labeled Band 1 consists of states built on an 8^+ level at 5344 keV. A double gate on the 939- and 960-keV transitions [see Fig. 4(b)] indicates the higher-lying γ rays in this structure, for example, the peaks at 1201, 1646, and 2847 keV, and the out-of-band decays via the 1457- and 1747-keV lines. The respective $J = 9$ and $10\hbar$ assignments to the 6284- and 7243-keV states result from the dipole character of the 939- and 960-keV γ rays. The levels at 8889 and 10090 keV are given tentative spin assignments of 11 and $12\hbar$, respectively, on the assumption that the 1646- and 1201-keV γ rays continue the trend of $\Delta J = 1\hbar$ transitions below, and that the 2606- and 2847-keV transitions are restricted to $\Delta J \leq 2\hbar$. The proposed spin assignments appear to be consistent with yrast feeding in the level scheme, given the intensity that the levels in Band 1 attract relative to others at similar energies in Bands 2 and 3, which are discussed later.

It is also noted that due to the presence of the in-band quadrupole transitions and the 1740-keV, $\Delta J = 2\hbar$

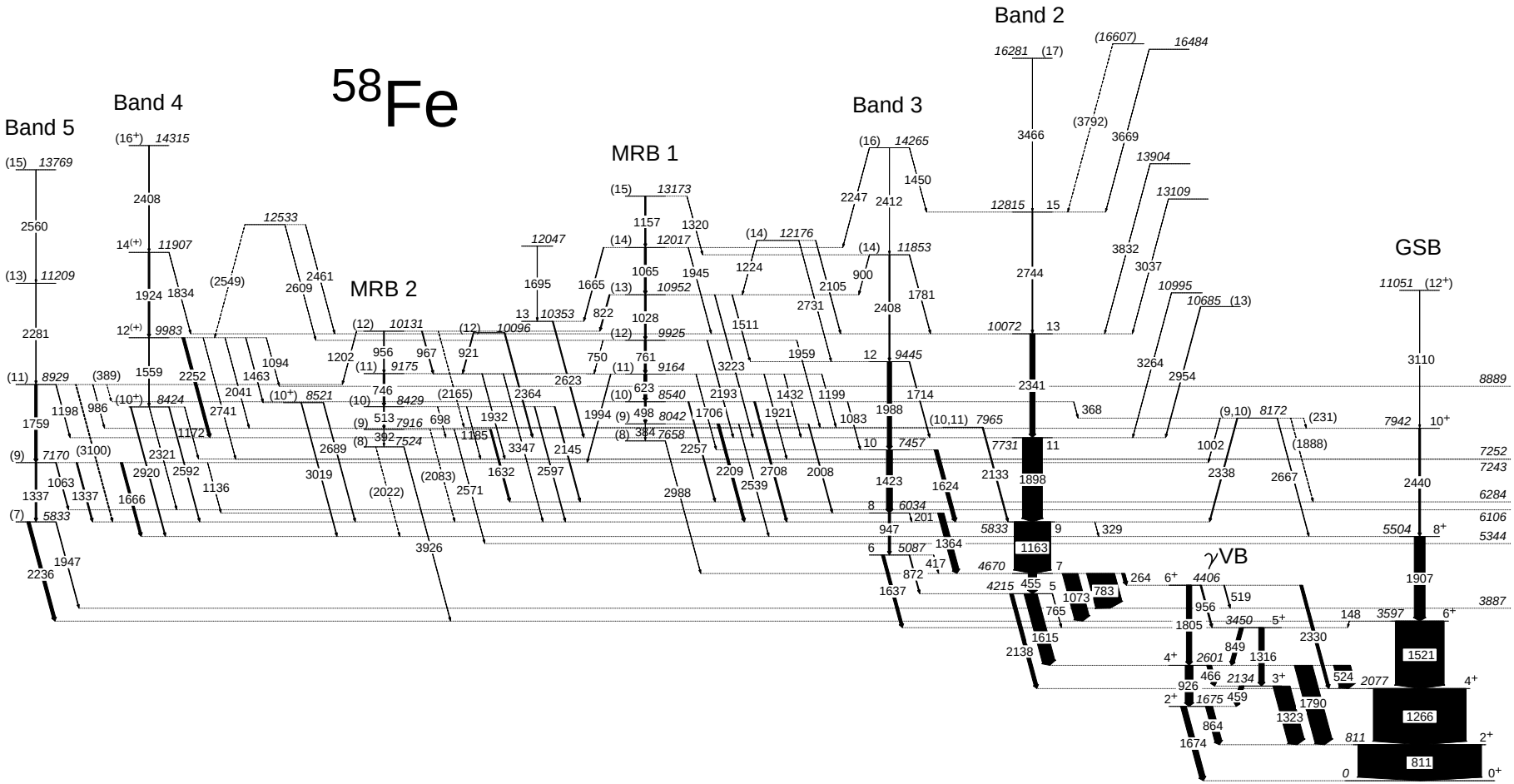

FIG. 2: Partial level scheme for ^{58}Fe deduced in the present study. Arrow widths are proportional to γ-ray intensities and tentative transitions are indicated by dashed lines and parentheses. The list of numbers (from 3887 to 8889 keV) to the right of the GSB are the energies of levels presented in Fig. 1 that are populated by γ rays displayed here. The GSB and γVB are reproduced from Fig. 1 to help indicate the feeding patterns of the bands at higher energy.

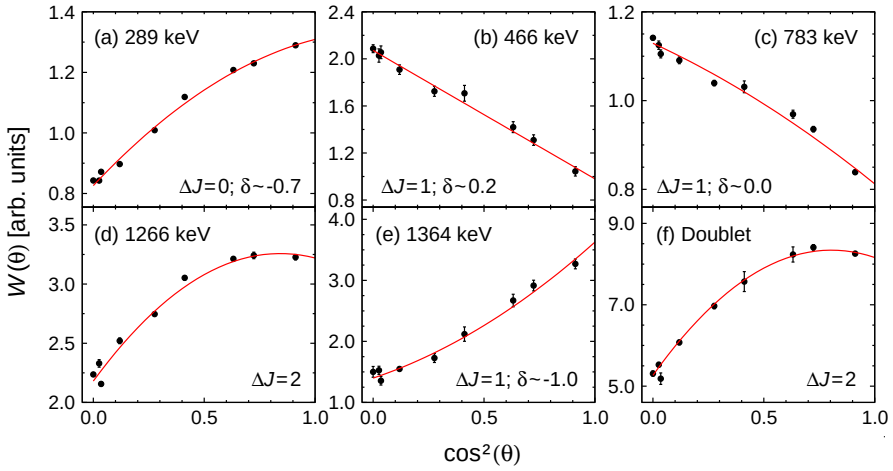

FIG. 3: (Color online) Angular distributions for the (a) 289-, (b) 466-, (c) 783-, (d) 1266-, (e) 1364-, and (f) summed intensity of the 1898/1907-keV transitions, which depopulate the levels at 3887, 2601, 4670, 2077, 6034, and 7731/5504 keV, respectively. The deduced spin change, ΔJ, and measured mixing ratio (where applicable), δ, of the γ-ray transition are indicated at the bottom of each panel.

out-of-band transition that populates the 8^+ state of the GSB at 5504 keV, a common parity is likely for Band 1. Therefore, the respective $J = 9 - 12\hbar$ levels from 6284 to 10090 keV have been tentatively assigned a positive parity based on the unambiguous spin-parity assignment of the 5344-keV state.

On the far right of the level scheme in Fig. 1 are numerous levels from which relatively weak transitions depopulate and feed Band 1 and the GSB. Several of these peaks are present in Fig. 4(b), such as the 2217-, 2453-, and 3676-keV lines, which are some of the most intense transitions in that part of the level scheme. Due to the observed feeding patterns of these states, i.e., the fact that they feed only into either the GSB or Band 1, these levels are candidates for non-yrast, positive-parity states.

The states discussed above have been investigated using the spherical shell model with several different effective interactions in the fp model space. The results are discussed in Section IV.

Bands 2 and 3. In previous studies, Band 2 was populated to $J = 15\hbar$ at 12.8 MeV [57, 58]. The present study confirms the placement of the 455-, 1163-, 1898-, 2341-, and 2744-keV γ rays, and extends the sequence via the 3466-keV transition (see Fig. 2). The in-band γ rays are indicated by Fig. 4(c), which displays a double energy gate on the 1163- and 1898-keV lines. The 264-, 783-, and 1073-keV transitions, which depopulate the level at 4670 keV in Fig. 2, were deduced here to be stretched $\Delta J = 1\hbar$ transitions and, therefore, the 4670-keV state is assigned $J = 7\hbar$. Similarly, the dipole character of the 1615-keV transition fixes the spin of the 4215-keV level as $J = 5\hbar$. The quadrupole nature of the 455-keV γ ray confirms the spin difference of $2\hbar$ between these two states, and the J^π assignments are in agreement with previous values [57, 58]. However, since the electric or magnetic character of the $\Delta J = 1\hbar$ transitions that depopulate Band 2 could not be deduced, the parity of the 4215- and 4670-keV levels cannot be given as a result. Previous studies on this matter are somewhat ambiguous: while the 4215-keV state was originally assigned negative parity from the ^{58}Fe(p,p$'$) reaction [64], the most recent compilation by Nesaraja *et al.* [57] tentatively assigns positive parity to the 4215- and 4670-keV levels from the fusion-evaporation study of Appelbe *et al.* [57, 58] and the results of ^{55}Mn(α,p) reactions [63, 65]. It is worthwhile noting that the non-observation of $\Delta J = 2\hbar$ transitions from Band 2 may suggest that a change of parity occurs, since the transition rates of the out-of-band quadrupole γ rays appear to be strongly hindered. This could, therefore, be an indication that relatively slow $M2$ transitions compete with faster $E1$ decays. In fact, similar decay characteristics have been observed, for example, in ^{55,57}Cr [2, 26], where quasirotational positive-parity bands were observed to decay only via $E1$ transitions to lower-lying negative-parity states. In contrast, however, the corresponding positive-parity band in ^{59}Cr decays via an $M2$ transition due to the fact that no $E1$ branch is available, and the $9/2^+$ bandhead state is isomeric in this specific case [15].

Before the remainder of the discussion, it is important to realize that there are in fact two levels in Fig. 2 with an energy of 5833 keV: one in Band 2, and another in Band 5, which is discussed later.

The series of four γ rays above the level at 4670 keV, up to and including the 12815-keV state, were all assigned a stretched-quadrupole character, which fixes the levels at 5833, 7731, 10072, and 12815 keV in Band 2 with $J = 9$, 11, 13, and $15\hbar$, respectively. These values are in agreement with the assignments in Refs. [57, 58], although the spin for the 12815-keV state was only tentatively assigned in those compilations. The 3466-keV γ ray, which is placed at the top of Band 2 in the present study, is assumed to continue the regular sequence of stretched

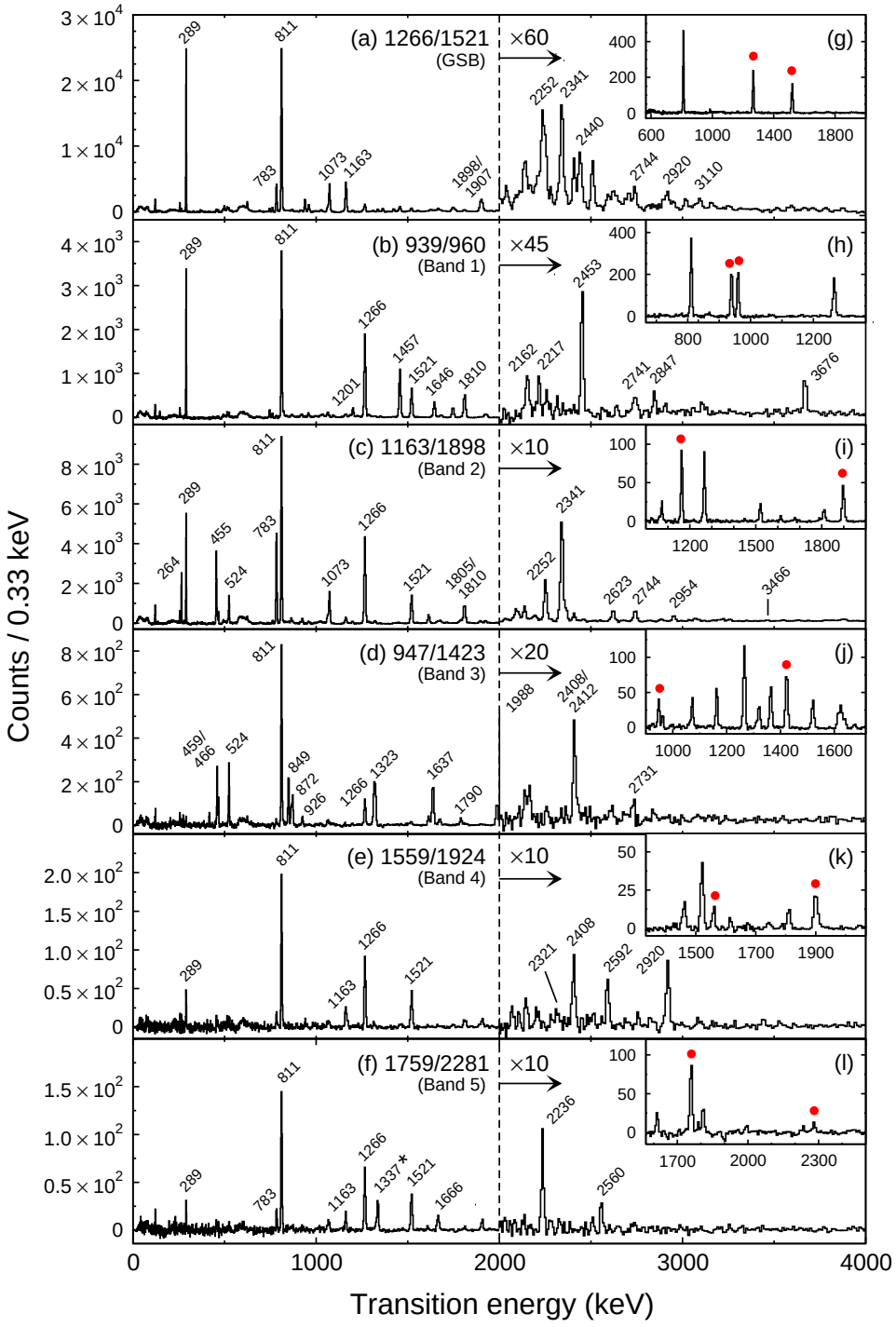

FIG. 4: (Color online) ^{58}Fe-gated coincidence spectra for (a) the GSB, and (b)–(f) Bands 1–5, respectively. Transition energies are given in keV, and the two numbers to the left of the dashed vertical line indicate the double energy gates. Note that the scale on the vertical axis changes at 2 MeV in Panels (a)–(f) to more clearly display weak transitions at higher energies. Insets (g)–(l) indicate the two gated peaks in Panels (a)–(f), respectively, which are marked by filled red circles; the energy gates used to produce the insets were (g) 1907/2440 keV, (h) 1201/1646 keV, (i) 2341/2744 keV, (j) 1988/2408 keV, (k) 1924/2408 keV, and (l) 1163/1337 keV. The transition marked with an asterisk (*) in Panel (f) is an unresolved doublet.

quadrupoles to $J = 17\hbar$ at 16281 keV.

Band 3, which begins from the 5087-keV state in Fig. 2, forms a series of stretched-quadrupole transitions that is composed of the 947-, 1423-, and 1988-keV γ rays; a double gate on the 947- and 1423-keV transitions is presented in Fig. 4(d), providing evidence for the higher-energy peaks in the band. The spins of the levels at 5087, 6034, and 7457 keV were investigated by measuring angular distributions and DCO ratios for the 1637-, 1364-, and 1624-keV transitions. While the 1637-keV line was found to be characteristic of a stretched-dipole transition [$R_{\rm DCO} = 0.59(4)$ when the energy gate is placed on the 947-keV quadrupole transition], resulting in a $J = 6\hbar$ assignment to the level at 5087 keV, the 1364- and 1624-keV lines were deduced to have significant mixing ratios ($\delta \sim -1.0$ and ~ 0.4, respectively) and, therefore, are likely to be folded $\Delta J = 0$ or $1\hbar$ transitions rather than stretched quadrupoles, which also have positive a_2 coefficients (see Table I). The angular distribution of the 1364-keV peak is provided in Fig. 3(e) as an example of one of the mixed transitions in Band 3. The 1364- and 1624-keV transitions are proposed to be of $\Delta J = 1\hbar$ character here, since the levels at 6034 and 7457 keV are assigned $J = 8$ and $10\hbar$, respectively, from the stretched-quadrupole nature of the 947- and 1423-keV γ rays.

Above 7457 keV in Band 3, the level at 9445 keV is unambiguously assigned $J = 12\hbar$, and the states at 11853 and 14265 keV are assigned tentative spins of 14 and $16\hbar$, respectively, on the assumption that each γ ray in the 2408/2412-keV doublet continues the sequence of $\Delta J = 2\hbar$ transitions that are present at lower energy.

In a similar way to Band 2, the parity of Band 3 could not be deduced since all of the γ rays that depopulate Band 3 are dipole transitions. It is also noted here that several crossover transitions are observed between Bands 2 and 3; i.e., the 1364-, 1624-, 1714-, 1781-, and 1450-keV γ rays. This is a characteristic consistent with a coupled band, and suggests that Bands 2 and 3 may represent favored and unfavored partners, respectively. This point will be examined further in Section IV.

Band 4. The 9983- and 11907-keV states in Fig. 2 were previously identified in the ^{48}Ca(^{13}C,3n) fusion-evaporation reaction by Appelbe *et al.* [57, 58]. The present study confirms the placements of the 2252- and 1924-keV transitions, and two new levels have been added to this band here: the 8424- and 14315-keV states. The 2408-keV transition and the out-of-band decays with $E_\gamma > 2$ MeV are presented in the 1559/1924-keV, double-gated spectrum of Fig. 4(e). Evidence for the placement of the 2252-keV line is provided in Fig. 4(c), since this transition populates the 7731-keV level in Band 2.

The multipolarities of the 2252- and 1924-keV transitions were investigated using a DCO ratio analysis and were assigned $\Delta J = 1$ and $2\hbar$, respectively. Note that not all DCO ratios are listed in Table I due to space restrictions; however, with an energy gate on the 2252-keV peak, for example, it was determined that $R_{\rm DCO} = 2.5(4)$ for the 1924-keV line, which is consistent with values for the 1163- and 1898-keV stretched-quadrupole transitions [$R_{\rm DCO} = 1.8(1)$ and 2.3(2), respectively]. Thus, the levels at 9983 and 11907 keV are assigned $J = 12$ and $14\hbar$, respectively, which confirms the tentative spin value suggested for the lower-energy state in Refs. [57, 58].

The 1559-keV in-band transition populates the level at 8424 keV, which decays out of Band 4 via four γ rays, two of which, the 2321- and 2920-keV lines, feed the respective $J^\pi = 8^+$ states at 6106 and 5504 keV. This restricts the spin-parity quantum numbers of the 8424-keV state to $J^\pi = 10^+$, assuming that the γ rays are limited to $\Delta J \leq 2\hbar$. Thus, since the parity of the lowest state in Band 4 is likely to be positive, the spins and parities of the higher-lying levels at 9983 and 11907 keV are assigned $J^\pi = 12^{(+)}$ and $14^{(+)}$, respectively. Furthermore, in a similar way to other bands already discussed, the highest-lying transition in the sequence, the 2408-keV line in the case of Band 4, is assumed to represent the natural extension of the stretched-quadrupole transitions to higher spin, and, therefore, the level at 14315 keV is tentatively assigned $J^\pi = 16^+$.

Band 5. All five states in Band 5 (see Fig. 2) are reported here for the first time. Figure 4(f) provides evidence for the placement of the new transitions, showing the results of a double energy gate placed on the 1759- and 2281-keV in-band transitions.

The spin-parity assignments in Band 5 are less certain than for other bands. The state at 5833 keV in Band 5 decays via the 1947- and 2236-keV γ rays to the $J^\pi = 6^+$ states at 3887 ($K = 6$ band) and 3597 (GSB) keV, respectively. Thus, the spin of the 5833-keV level in Band 5 is restricted to either $J = 6$, 7, or $8\hbar$, based on the assumption that the γ rays are limited to $\Delta J \leq 2\hbar$. Since fusion-evaporation reactions preferentially populate states close to the yrast line, an assignment of $J = 6\hbar$ seems rather unlikely as the state would lie more than 2.2 MeV above the yrast 6^+ state at 3597 keV in the GSB. Furthermore, an assignment of $J = 8\hbar$ seems unreasonable since the 5833-keV level in Band 5 would then lie closer to the yrast line than the state at 6034 keV in Band 3, while attracting much less feeding according to the γ-ray intensities. Therefore, given the above discussion, the state at 5833 keV (Band 5) is tentatively assigned $J = 7\hbar$ in the present work. Similar arguments were used to assign $J = 9\hbar$ to the level at 7170 keV.

The multipolarities of the in-band transitions, the 1337-, 1759-, 2281-, and 2560-keV γ rays, could not be investigated due to their relatively low intensities. However, given the similarity in the general structure of Band 5 with other quasirotational bands in the level scheme, the states at 8929, 11209, and 13769 keV have been assigned tentative values of $J = 11$, 13, and $15\hbar$, respectively, on the assumption that Band 5 is also a regular sequence of stretched-quadrupole transitions. Note that with these spin assignments, Band 5 does

TABLE II: DCO ratios for γ rays in MRB 1. The 783- and 1521-keV peaks are included as reference values in the final two columns for stretched-dipole (d) and stretched-quadrupole (q) transitions, respectively.

E_γ gate	Transition energy (keV)					
(keV)	498	623	761	2708	$783^{(d)}$	$1521^{(q)}$
498	–	1.00(4)	1.00(7)	–	0.96(5)	1.83(8)
623	0.97(5)	–	1.05(4)	1.10(12)	0.88(3)	1.74(4)
761	1.09(11)	0.93(4)	–	1.03(18)	0.88(3)	1.76(6)

not reach the yrast line, in agreement with the relative intensities of the four in-band transitions.

MRB 1 and MRB 2. All levels and γ rays in the bands labeled MRB 1 and MRB 2 in Fig. 2 are reported here for the first time. Evidence for the transitions and their placements in the level scheme is proposed in Fig. 5, which displays various double-gated energy spectra. In Fig. 5(a), gates are applied on the 623- and 761-keV transitions in MRB 1, indicating their coincidence relationships with the 498-, 1028-, 1065-, and 1157-keV in-band peaks, and several out-of-band transitions at 368, 2008, 2209, 2257, and 2708 keV, which connect MRB 1 to other parts of the level scheme. The 1065- and 1157-keV lines form unresolved doublets with the relatively intense 1073- and 1163-keV transitions that depopulate the respective 4670- and 5833-keV levels in Band 2, and it is noted that an increase in the widths of these unresolved lines is observed relative to the other peaks in the spectra. Figure 5(b) provides a double gate on the 498- and 2209-keV transitions, which presents several peaks absent in Fig. 5(a), for example, the lines at 623, 761, and 967 keV. Finally, in Fig. 5(c), the double gate on the 746- and 956-keV transitions in MRB 2 displays the other strong in-band line at 513 keV, and numerous out-of-band decays such as the peaks at 1632, 2145, and 2597 keV. Furthermore, Fig. 5(c) indicates that MRB 1 and MRB 2 are connected via the 822-keV transition, which can be more clearly seen in the expanded spectrum of Fig. 5(e).

The spins of the states in these bands were investigated using DCO ratios, which are provided in Table II. Although the DCO values measured using a 623-keV gate have been included in the table, they must be treated with caution since ^{74}Ge(n,n$'$) peaks, which are present at $\sim$ 600 keV [66], contaminated the energy gate in this specific case.

The DCO ratio for the 2708-keV γ ray, which depopulates the level at 8540 keV in MRB 1 and feeds the $J = 9\hbar$ state at 5833 keV in Band 2, is consistent with those expected for a stretched-dipole transition ($R_{\rm DCO} \sim 1.0$), and the 8540-keV state has been assigned $J = 10\hbar$. However, since the uncertainties of the DCO ratios are relatively large, the spin is only given as a tentative assignment. Furthermore, energy gates at 498, 623, and 761 keV result in $R_{\rm DCO} \sim 1.0$ for the 623/761-, 498/761-, and 498/623-keV peaks, respectively, indicating that these three γ rays are all characteristic of stretched-dipole transitions (see Table II for details). Thus, the levels at 8042, 9164, and, 9925 keV, have been assigned $J = 9$, 11, and $12\hbar$, respectively.

The $J = 9\hbar$ assignment to the 8042-keV level in MRB 1 indicates that the 2209-keV transition is of $\Delta J = 0$ character. DCO ratios from gates on the 498-, 623-, and 761-keV lines are $R_{\rm DCO} = 1.9(2)$, 1.3(2), and 1.5(4), respectively: since these are all consistent with typical values for stretched-quadrupole transitions, it is suggested that the 2209-keV γ ray is a mixed $\Delta J = 0$ transition with a significant quadrupole component.

Deducing DCO ratios for the higher-lying transitions, the 1028-, 1065-, and 1157-keV lines, was difficult due to the ^{27}Al(n,n$'$) peak at 1014 keV [66], relatively low γ-ray intensities, and contamination from the unresolved transitions at 1073 and 1163 keV. The tentative $J = 13-15\hbar$ assignments in MRB 1 are proposed by assuming that the three γ rays at the top of the band continue the trend of $\Delta J = 1\hbar$ transitions observed at lower energy, and that the out-of-band γ rays that depopulate MRB 1 are limited to $\Delta J \leq 2\hbar$. The tentative $J = 8\hbar$ assignment to the state at 7658 keV was deduced using similar arguments.

Spin-parity assignments for the levels of MRB 2 were also rather difficult. DCO ratios extracted from an energy gate at 746 keV are $R_{\rm DCO} = 0.84(9)$, 1.05(12), and 0.89(14), for the 822-, 956-, and 2145-keV γ rays, respectively, which suggests a common multipolarity for these transitions. Based on the general similarity between the structures of MRB 1 and MRB 2, i.e., both exhibit regular sequences of relatively low-energy γ-ray transitions with comparable intensities between the bands, it is assumed that MRB 2 is also characterized by a series of stretched-dipole transitions, which in turn suggests that the 2145-keV γ ray that populates the $J = 9\hbar$ state at 6284 keV in Band 1 also has a $\Delta J = 1\hbar$ character. As a result, the levels at 8429, 9175, and 10131 keV are tentatively assigned $J = 10$, 11, and $12\hbar$, respectively.

A DCO ratio for the 513-keV γ ray could not be obtained due to contamination from e^+e^- annihilation, which becomes "smeared" around 511 keV after correcting the energies of Doppler-shifted peaks in γ-ray spectra. Moreover, the relative intensity of the 392-keV line at the bottom of MRB 2 was too low to measure DCO ratios. However, by assuming that the 392- and 513-keV transitions are of the same multipolarity as the other in-band transitions of MRB 1 and MRB 2, the levels at 7524 and 7916 keV have been tentatively assigned $J = 8$ and $9\hbar$, respectively. Furthermore, the 1632-keV transition, which depopulates the 7916-keV level in MRB 2 and feeds the $J = 9\hbar$, 6284-keV state in Band 1, has $R_{\rm DCO} = 1.7(3)$ when the energy gate is placed on the 746-keV line, indicating that it likely is a $\Delta J = 0$ transition of mixed character, similar to the 2209-keV γ ray that depopulates MRB 1.

Finally, it is noted that the relative γ-ray intensities in MRB 1 and MRB 2 appear to be consistent with yrast

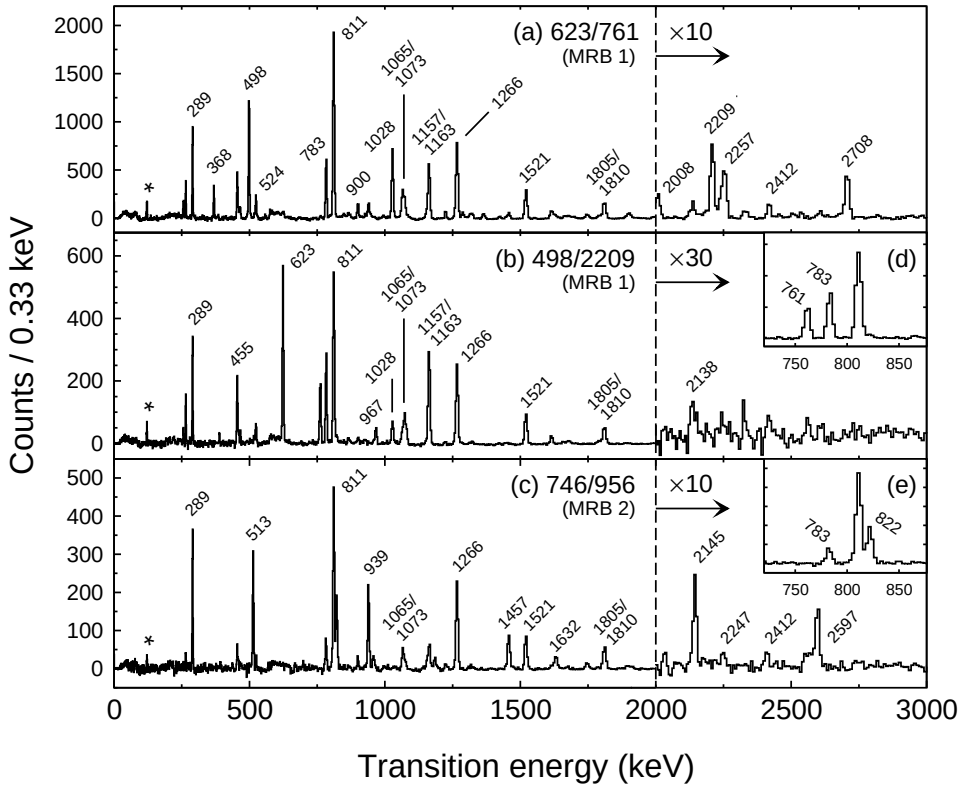

FIG. 5: ^{58}Fe-gated coincidence spectra for MRB 1 and MRB 2. Transition energies are given in keV and the two numbers to the left of the dashed vertical line indicate the energies of the double gates. Note that the scale on the vertical axis changes at 2 MeV in Panels (a)–(c) to more clearly display weak transitions at higher energies. Insets (d) and (e) provide a zoomed region around 800 keV to more clearly identify the 761- and 822-keV transitions in Panels (b) and (c), respectively; the scale on the vertical axis is unchanged. The low-energy transition marked with an asterisk (*) is a contaminant from ^{57}Fe.

feeding given the spin assignments proposed above, and that the $\Delta J = 1\hbar$ crossover transitions, the 750-, 822-, and 967-keV γ rays, occur between $J = 11 - 13\hbar$, the point at which MRB 1 crosses MRB 2 and, accordingly, moves closer to the yrast line.

IV. DISCUSSION

A. The ground-state band, Band 1, and other positive-parity states

The candidate positive-parity states are compared to predictions of the GXPF1A [12], KB3G [13], and FPD6 [14] effective interactions in Fig. 6. The calculations were performed using the codes NuShellX [67] and MSHELL64 [68]. All three interactions were applied in the fp-shell model space with a ^{40}Ca core and $t = 6$ truncation, which defines the allowed configuration $f_{7/2}^{n-t} r^{m+t}$, where r represents the proton and neutron orbitals $f_{5/2}$, $p_{3/2}$, and $p_{1/2}$, n is the maximum number of nucleons allowed in the $f_{7/2}$ orbital, and m is the minimum number of nucleons allowed in the r subset of orbitals; these numbers are $n = 14$ and $m = 4$ in the case of ^{58}Fe. Thus, t is the maximum number of nucleons excited from $f_{7/2}$ to r, i.e., across the Z and $N = 28$ shell closures. This truncation was introduced to make the calculations more tractable. However, it is noted that at intermediate to high spin, where it was easier to perform the full calculations, the effect of the truncation is not significant ($\lesssim 10$ keV change in level energy).

It is clear that, at relatively low energy ($\lesssim 3$ MeV), all three Hamiltonians reproduce the experimental data rather well. However, the predictions of the FPD6 interaction, presented in Fig. 6(d), start to deviate quite substantially from the experimental results, even at relatively low spin. For example, the yrast 5^+ and second 4^+ states lie 504 and 420 keV, respectively, above their experimental counterparts, while, in contrast, the GXPF1A and KB3G Hamiltonians continue to reproduce the experimental energies successfully up to, and including, $J = 8\hbar$. The KB3G interaction then begins to deviate from the experimental values at $J = 9\hbar$.

To quantify the discrepancies, the root-mean-square (rms) deviation between experimental and calculated states, $\Delta_{\rm rms}$, was used, which is defined as

$$\Delta_{\rm rms} = \sqrt{\frac{1}{N}\sum_{i=1}^{N}\left(E_{\rm Exp}^{(i)} - E_{\rm SM}^{(i)}\right)^2}, \qquad (4)$$

where $E^{(i)}_{\rm Exp}$ and $E^{(i)}_{\rm SM}$ represent the energy of the i-th experimental and shell-model levels, respectively, and N is the total number of states included in the calculation. For the nine experimental levels below 5 MeV (not including the ground state) in Fig. 1, which lie in the spin range $J = 2 - 6\hbar$, the rms deviation between the corresponding experimental and calculated levels for the GXPF1A and KB3G Hamiltonians are very similar ($\Delta_{\rm rms} = 57$ and 55 keV, respectively). However, when all experimental excited states below 8 MeV in Fig. 1 are included, the rms deviation increases rather significantly in the case of the KB3G interaction ($\Delta_{\rm rms} = 201$ keV), whereas the value for GXPF1A effectively remains the same ($\Delta_{\rm rms} = 58$ keV). The $J^\pi = 8^+$, 9^+, and 10^+ states predicted by the FPD6 Hamiltonian deviate even further from the experimental values. For example, the yrast state for each of these spins lies 436, 592, and 536 keV above its experimental counterpart, respectively, and the rms deviation for all positive-parity experimental states below 8 MeV is 531 keV.

For $J^\pi \geq 10^+$, the differences between the three shell-model interactions become clearer. The energies of the yrast states highlight this point well, since the $J^\pi = 10^+_1 - 15^+_1$ states of the FPD6 Hamiltonian lie 482, 326, 431, 1091, 309, and 693 keV, respectively, *above* the GXPF1A predictions, while the same levels of the KB3G interaction lie 406, 548, 522, 260, 540, and 638 keV, respectively, *below* the GXPF1A values. Above 8 MeV, however, the comparison between the experimental levels and the predictions of the shell-model interactions becomes rather difficult since no firm spin-parity assignments are available [see Fig. 6(a)].

It is noted that the $J^\pi = 11^+$ and 12^+ levels at 8889 and 10090 keV in Band 1, which were assigned tentative spin values on the assumption that there is a continuation in the sequence of $\Delta J = 1\hbar$ transitions to higher spin, are reproduced rather well by the GXPF1A interaction (they lie 142 and 87 keV from their experimental counterparts, respectively), giving some support to these assignments.

The calculations with all three Hamiltonians for the $J^\pi = 0^+ - 10^+$ states in the GSB are dominated by the $\pi[(f_{7/2})^{-2}] \otimes \nu[(f_{7/2})^8(p_{3/2})^2(f_{5/2})^2]$ configuration (hereafter labeled Config. A), with contributions in the range $16\% - 28\%$, $26\% - 51\%$, and $15\% - 32\%$ for the GXPF1A, KB3G, and FPD6 interaction, respectively.

Furthermore, the GXPF1A and KB3G interactions predict that the states in Band 1, which crosses the GSB at around $J = 8\hbar$, are dominated by the $\pi[(f_{7/2})^{-2}] \otimes \nu[(f_{7/2})^8(p_{3/2})^3(f_{5/2})^1]$ configuration (Config. B), at levels of approximately $30\% - 40\%$ up to the $J^\pi = 10^+$ state at 7243 keV. Here, the maximum spin available from Config. B is exhausted. At higher spins in Band 1, for example, for the yrast $J^\pi = 11^+$ and 12^+ states, Config. A dominates with contributions as high as 50% or more at $J = 12\hbar$. However, since the maximum spin that can be achieved from Config. A is $12\hbar$, the higher-lying states are likely to be dominated by additional contributions from other configurations.

It is also noted that the non-observation of the $7243 \rightarrow 5344$-keV γ ray in Band 1 of Fig. 1 is best reproduced by the KB3G interaction, which predicts a $B(E2; 10^+_1 \rightarrow 8^+_1)$ reduced transition rate that is a factor ~ 0.1 of $B(E2; 10^+_1 \rightarrow 8^+_2)$. In contrast, the GXPF1A and FPD6 Hamiltonians predict that the feeding to the yrast 8^+ state is the larger of the two branches, by factors ~ 2.2 and ~ 4.8, respectively, indicating that both of these interactions are inconsistent with the experimental result in this specific instance.

Moreover, the decay pattern from the yrast 8^+ level (the experimental level at 5344 keV in Band 1) highlights further inconsistencies between the different shell-model results and experimental values. On the one hand, the KB3G Hamiltonian predicts a stronger feeding to the 6^+_2 state relative to the yrast 6^+ level, but the ratio of the predicted strengths (~ 70) is much larger than observed in the experimental level scheme (~ 3). The KB3G interaction also predicts a decay branch to the 6^+_3 state that is comparable to that to the 6^+_2 level, but such a transition was not observed in the experimental data (with an experimental limit $I_\gamma \lesssim 0.01$).

On the other hand, the GXPF1A Hamiltonian predicts a very small decay branch to the 6^+_3 state, which better suits the experimental non-observation, but suggests that the feeding into the yrast 6^+ state is ~ 2.6 times larger than that to the 6^+_2 state, which disagrees with the experimental results, but in a different manner than the case for KB3G. The general decay pattern predicted by the FPD6 interaction is similar to that of the GXPF1A Hamiltonian in this instance, although the discrepancy with the experimental results is more extreme.

The results of the present study generally suggest that the GXPF1A interaction is the more successful of the three shell-model Hamiltonians tested, at least over the subset of states reported here. Nevertheless, discrepancies in all three shell-model interactions with the experimental data are clear from the predicted transition rates. Furthermore, firm spin-parity assignments to the levels at higher energy (8 MeV and above) are required before any statement can be made about the ability of the three Hamiltonians to reproduce the high-spin states in ^{58}Fe. Several previous studies [16, 26, 27, 29] have indicated that the influence of the $\nu g_{9/2}$ intruder orbital becomes important, particularly at high spin, which effectively causes a compression of the experimental states relative to shell-model predictions that are restricted to the fp model space. This highlights the need to expand the calculations to a larger model space, even for nuclei at stability; some recent progress has been made, see for example, Refs. [20, 23, 24, 69].

Subtle structural changes and differences between rotational bands can be emphasized by using the rotational frequencies of the bands, which involve a derivative of the level energy with respect to the angular momentum [43]. In Fig. 7(a), the experimental rotational frequency ($\hbar\omega_{\rm exp}$) is plotted as a function of aligned angular momentum (J_x) for the GSB. It is interesting

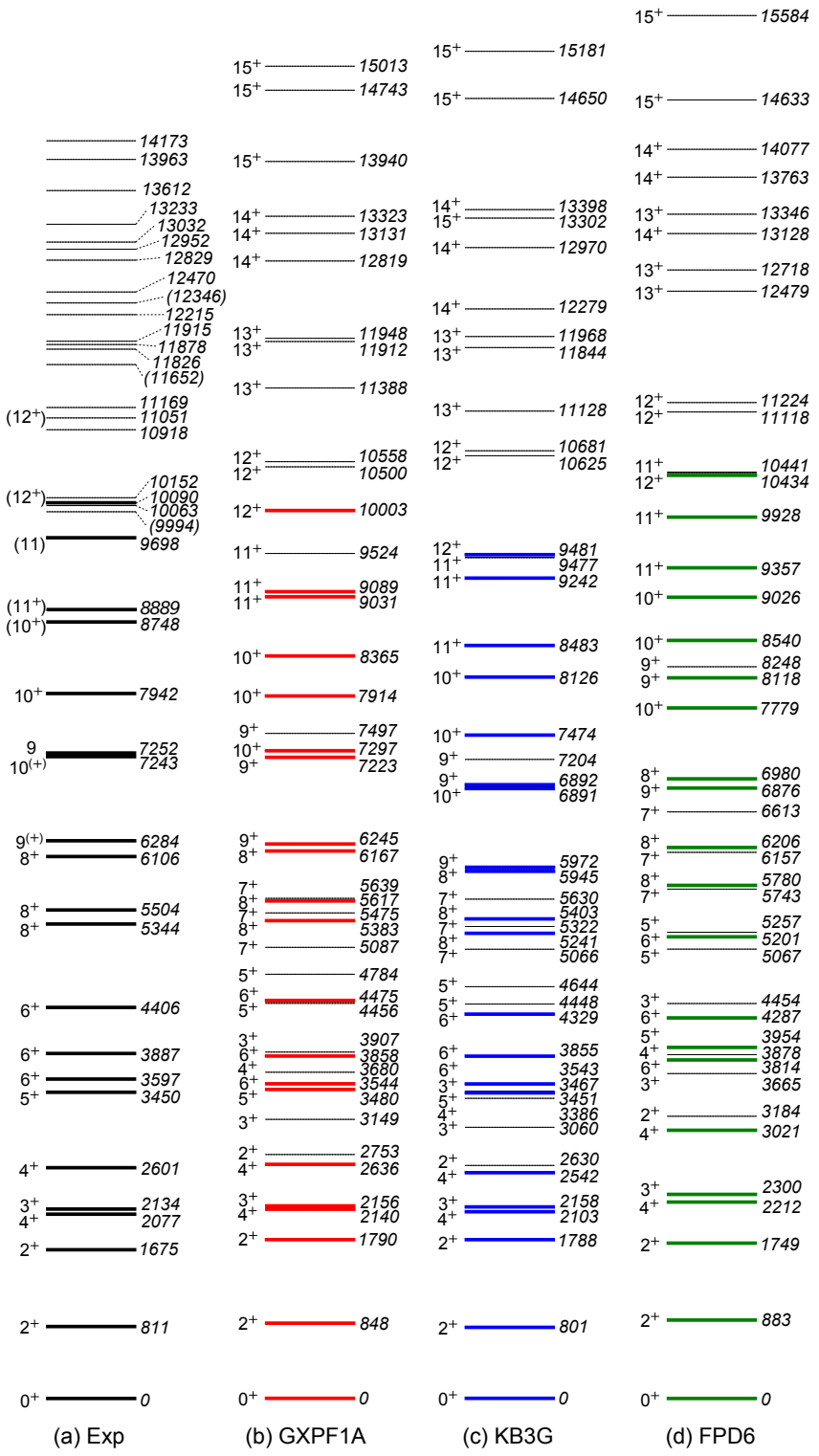

FIG. 6: (Color online) Candidate positive-parity experimental energy levels [Column (a)] compared to predictions of various effective interactions in the fp model space. Only the first three states for each spin are presented for the calculations; levels with $J^\pi = 0^+$ or 1^+, with the exception of the ground state, have been omitted from Columns (b), (c), and (d) to aid clarity in the figure. The thick colored lines for the shell-model predictions represent the corresponding states of the thick lines in Column (a), and are intended to help guide the eye. Calculated levels in black have no assigned experimental counterparts here.

to note that the maximum spin-parity available from the $\pi[(f_{7/2})^{-2}] \otimes \nu[(p_{3/2}f_{5/2}p_{1/2})^4]$ configuration is 12^+, which matches the highest spin suggested by the experimental level scheme. However, it is evident from the band diagram in Fig. 7(a) that the distribution of the experimental data points stays relatively linear and does not deviate or bend significantly at the expected termination point of the GSB configuration.

The projected shell model [22] was also applied in the present study to investigate the GSB. As discussed in detail in Ref. [23], the theory is based on the deformed Nilsson model [70], where respective quadrupole and hexadecapole deformation parameters of $\epsilon_2 = 0.230$ and $\epsilon_4 = 0.027$ were adopted for the ^{58}Fe calculations. The experimental data are plotted with the 0-quasiparticle (qp), $K = 0$ band, i.e., the prediction of the unmixed ground-state band by the PSM, in Fig. 7(b), which is reproduced here from Ref. [23] to aid the following discussion. While the general trend of the data points is reproduced well, the theory appears to deviate from experiment at higher spin. However, it is stressed that the PSM band displayed in Fig. 7(b), and also for those in Figs. 7(c) and 7(d) that will be discussed later, represents results for pure angular-momentum-projected qp configurations, before configuration mixing is performed, and such deviations from the experimental data are, therefore, not too surprising. Despite this, the unmixed bands are still capable of reproducing the general trends of the experimental bands, and such qualitative comparisons are the main intention of the present study, rather than a detailed quantitative test. In fact, the yrast states presented in Ref. [23], which were obtained after performing configuration mixing of the most important qp configurations, should be used for that specific purpose.

It is also worthwhile noting that, since only one set of deformation parameters was used for constructing the PSM model basis, which were chosen to optimize the study of high-spin quasirotational bands based on $\nu g_{9/2}$ configurations, one might naïvely expect discrepancies with the experimental GSB, which was described using only fp-shell configurations. Indeed, the predictions of total-Routhian-surface (TRS) calculations for ^{59}Fe [29] indicate that neutron excitations involving the $\nu g_{9/2}$ orbital can change the magnitude of the prolate and triaxial deformation parameters, and, therefore, one might expect similar changes to occur for ^{58}Fe as well. In fact, previous PSM and TRS calculations have already highlighted this point for ^{55}Cr [31].

B. The $K^\pi = 6^+$ band

In Ref. [23], the $J^\pi = 6^+$ level at 3887 keV was interpreted as the bandhead state of a $K^\pi = 6^+$, 2-qp proton configuration involving the $\Omega = 5/2$ and 7/2 Nilsson states of $\pi f_{7/2}$ spherical parentage. Since the proton Fermi surface lies between these two deformed states, the $K = 6$ band appears at relatively low energy (see Fig. 1 in Ref. [23] for details), and, therefore, can be accessed experimentally in reactions such as those reported here.

Since the higher-spin states of the $K = 6$ band are predicted to rise rather rapidly according to the band diagram in Fig. 5 of Ref. [23], only the theoretical $J^\pi = 6^+$ and 8^+ members of the band were discussed previously, as those were considered to be the most likely to be observed experimentally.

The experimental $J^\pi = 8^+$ level at 6106 keV, which feeds the 3887-keV level via the 2220-keV, $\Delta J = 2\hbar$ transition, is one possible candidate for the $J = 8\hbar$ member of the $K = 6$ band. Furthermore, the $J^\pi = 10^+$ state at 8748 keV may represent the continuation of this band to higher spin, although the 2640-keV γ ray is only placed as a tentative transition in the level scheme of Fig. 1. These three experimental levels are plotted against the prediction of the PSM in Fig. 8. In a similar way to the calculated values previously discussed for Fig. 7(b), the energy levels of the unmixed π 2-qp, $K = 6$ configuration are presented. In this specific instance, however, it is worthwhile noting that the $K = 6$ band does not mix significantly with the other configurations investigated in Ref. [23].

The energy of the lowest member of the band, the $J^\pi = 6_2^+$ experimental state, is reproduced rather well by the PSM. Despite the fact that the higher-lying states are predicted at slightly higher energies than the experimental values, the general trend of the experimental states is reproduced in a satisfactory manner. In particular, the approximate linearity of the points is accounted for. The 3887-, 6106-, and 8748-keV states are, therefore, suggested to be experimental counterparts of the $K^\pi = 6^+$ band. As mentioned by the authors of Ref. [23], measurements of experimental g-factors would provide one means to clarify the true nature of these states.

C. Bands 2 and 3

The quasirotational bands built above the respective $J = 5$ and $6\hbar$ levels at 4215 and 5087 keV were also investigated with the PSM. Band 2 was studied in a similar way in Ref. [23], but the extension of Bands 2 and 3 here allows for a more extensive test of the predictions at higher spin.

In Fig. 7(a), $\hbar\omega_{\rm exp}$ versus J_x is displayed for the experimental data of these two bands. It is interesting to note the similarity in the general trend of the plots between Band 2 and the GSB, and the fact that each of the seven states in Band 2 has $5\hbar$ units of angular momentum more than the corresponding level in the GSB. This band could, therefore, be naïvely interpreted as the coupling of the GSB to a higher-lying single-particle configuration.

In order to investigate the nature of Band 2 further, predictions of the PSM were used. These calculations are presented in Fig. 7(c), reproduced from Fig. 8 of Ref. [23] to aid the following discussion. These represent calculated levels for the favored and unfavored signature

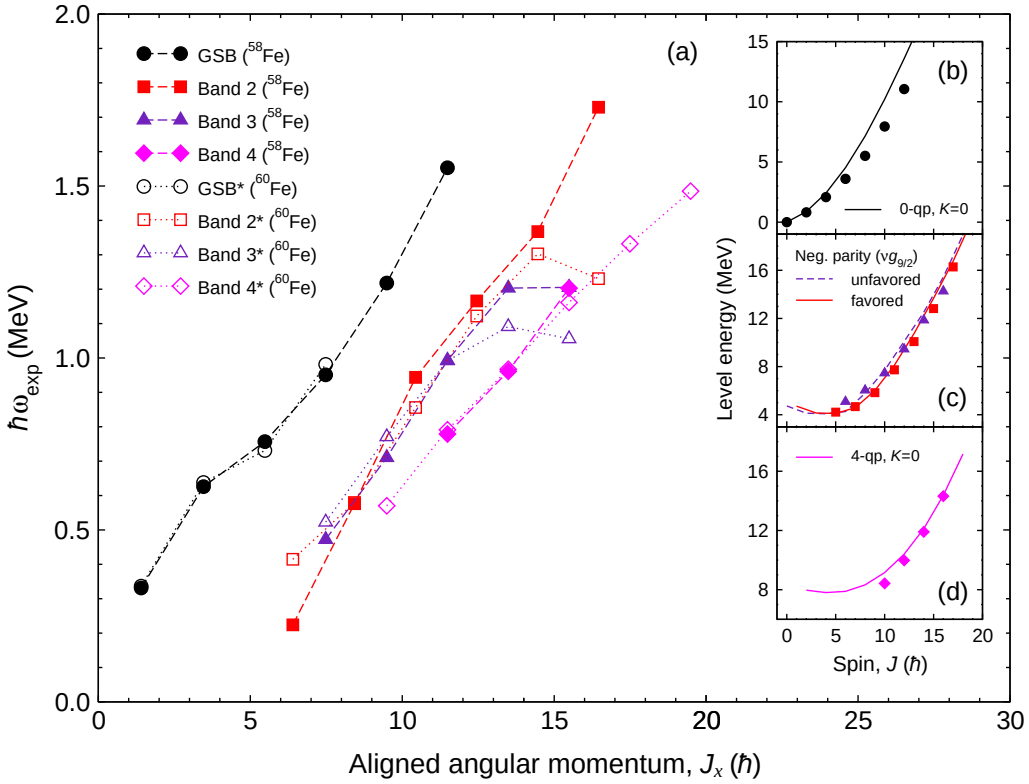

FIG. 7: (Color online) (a) Experimental rotational frequency ($\hbar\omega_{\rm exp} = {\rm d}E/{\rm d}J_x$) as a function of aligned angular momentum ($J_x = [J(J+1) - K^2]^{1/2}$) for various bands deduced in the present study (filled symbols) and their counterparts in ^{60}Fe (open symbols) [29]. The dashed lines are intended to guide the eye. The experimental spin is plotted against level energy for (b) the GSB, (c) Bands 2 and 3, and (d) Band 4, respectively. The solid and dashed lines are predictions of the PSM, reproduced from Ref. [23] (see text for details).

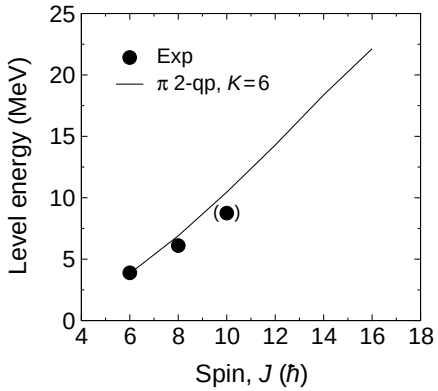

FIG. 8: Experimental data deduced in the present study (filled black circles) for the proposed $K^\pi = 6^+$ band in ^{58}Fe. The parentheses indicate a tentative assignment, and the solid line is the prediction of the PSM, reproduced from Ref. [23].

partners of a 2-qp, negative-parity configuration with one neutron qp occupying a low-Ω state of the $\nu g_{9/2}$ parent orbital, namely the $\Omega = 1/2$ or $3/2$ Nilsson state, and the other neutron qp occupying the fp shell, namely the $\Omega = 1/2$ state of the $\nu f_{5/2}$ orbital or the $\Omega = 3/2$ state of the $\nu p_{3/2}$ orbital (see Fig. 1 of Ref. [23] for the relevant Nilsson diagrams).

In both cases, the general trend of the experimental data points is reproduced well by the PSM, although the agreement tends to deviate slightly at higher spins, from around $J \sim 12\hbar$, in a way similar to the GSB. There is also a small deviation at $J = 6\hbar$ for the unfavored signature.

Based on the PSM interpretation above, the parity of Bands 2 and 3 is negative, which supports the simple argument discussed in Section III regarding the possible assignment of negative parity to Band 2. However, it is stressed that further work on the experimental front, for example, measurements of γ-ray polarization coefficients for the $\Delta J = 1\hbar$ transitions from the $J = 5$ and $7\hbar$ levels of Band 2, is required to confirm this statement.

It was proposed by Sun *et al.* [23] that the lowest-spin states of the 2-qp, negative-parity bands in the Fe isotopes are either degenerate with the $J^\pi = 5^-$ level or lie at higher energy. Therefore, these states would lie rather far from the yrast line, and would not be populated strongly in fusion-evaporation reactions. This suggests that the $J = 5$ and $6\hbar$ levels at 4215 and 5087 keV are not bandhead states, and that the K quantum numbers of the coupled bands may in fact be relatively low ($K = 0$, 1, or 2), as one might expect from a coupling of the low-Ω

Nilsson states discussed above.

In fact, the PSM indicates that the energetically favored 2-qp, negative-parity band becomes yrast over the positive-parity states at $J \sim 7\hbar$, in good agreement with the experimental level scheme. Furthermore, this band is expected to cross the GSB around $J = 5\hbar$, and despite the fact that this is not observed experimentally, the $J^\pi = 5^-$ level of Band 2 does lie sufficiently close to the yrast line to be populated in fusion-evaporation reactions.

Overall, the PSM provides a satisfactory description of Bands 2 and 3 as the favored and unfavored signature partners of the aforementioned 2-qp, negative-parity band.

D. Band 4

The $J = 14$ and $16\hbar$ members of Band 4 lie close in energy to levels with the same spin in Band 3, and approach the yrast line, which is governed by Band 2 at intermediate to high spin, around $J = 16\hbar$. In contrast, the two lower-spin members of Band 4, the $J^\pi = 10^+$ and 12^+ levels at 8424 and 9983 keV, respectively, lie much further from the yrast line, indicating that the band only becomes energetically favored at high spin. This point is emphasized by the drop in intensity of the 1559-keV peak relative to the line at 1924 keV. As discussed previously for Bands 2 and 3, the lowest member of the band is not necessarily the bandhead state, but probably results as a consequence of band crossings and the yrast feeding of the fusion-evaporation reaction.

To investigate this point further in this case as well, the experimental data were compared to PSM predictions, which are presented in Fig. 7(d). The 4-qp, $K = 0$ band reproduces the experimental points rather well, although the value at $J = 10\hbar$ deviates a little from the experimental value. It is also noted that the theoretical curve begins to flatten out below $J \sim 10\hbar$, causing these states to lie relatively far from the yrast line. This feature provides a plausible explanation for the non-observation of the $J \leq 8\hbar$ members of Band 4 in the experimental level scheme. The PSM also predicts a band crossing between the 4-qp band and the neutron 2-qp, negative-parity band near $J = 14\hbar$, in excellent agreement with the experimental observation.

According to the PSM, the 4-qp, $K = 0$ band results from a coupling of a neutron 2-qp, $K = 1$ configuration with positive parity, which mainly involves the $\Omega = 1/2$ and 3/2 states from the $\nu g_{9/2}$ parent orbital, with a proton 2-qp, $K = 1$ state that involves the $\Omega = 5/2$ and 7/2 states of the $\pi f_{7/2}$ orbital. In fact, the $K = 6$ coupling of the latter configuration was the one discussed in Section IV B.

Finally, it is noted that the parity of the theoretical 4-qp band discussed here is positive, which supports the tentative parity assignments proposed in the present study for Band 4 (see Section III).

E. Band 5

In the spin range populated in the present work, $J \sim 7 - 15\hbar$, Band 5 does not become yrast. This makes its interpretation more difficult due to the numerous non-yrast configurations displayed in Fig. 5 of Ref. [23] that could, in principle, lie close enough to the yrast line to have been populated experimentally.

In fact, the empirical data points for the five levels in Band 5 lie between the theoretical curves for the yrast states and the 4-qp, $K = 0$ band, which correspond to Bands 2 and 4, respectively. This appears to rule out the possibility of configurations such as the proton and neutron 2-qp, $K = 1$ bands in the fp shell (see Fig. 5 in Ref. [23] for details), and Band 5 may involve configurations that were not investigated in Ref. [23].

F. Corresponding bands in ^{60}Fe

In addition to the results obtained in the present study, Fig. 7(a) also gives aligned angular momenta plots for several bands in the even-even neighbor ^{60}Fe, which was recently reported by Deacon *et al.* [29].

There are several striking similarities between the two isotopes. Firstly, the sequence of transitions in the ground-state band up to the 8^+ level, which corresponds to the 2^+, 4^+, 6^+, and 8^+ states at 824, 2114, 3582, and 5549 keV, respectively, in ^{60}Fe (labeled GSB* in Fig. 7), lie very close to their counterpart levels in ^{58}Fe. The two additional points that correspond to the extension of the GSB to $J^\pi = 10^+$ and 12^+ in the present study appear to have no obvious counterparts in ^{60}Fe, which suggests that these higher-spin states in GSB* lie further from the yrast line than they do in ^{58}Fe.

In both isotopes, a discontinuity is observed in the positive-parity states beyond $J = 8\hbar$, i.e., beyond the 5344- and 5333-keV levels in ^{58,60}Fe, respectively. One might, therefore, expect similar configurations to be responsible for these abrupt changes. However, there are several distinct differences between the two cases that must be considered. Firstly, while the GXPF1A Hamiltonian reproduces the $J^\pi = 10^+_1$ state in ^{58}Fe very well, the same level in ^{60}Fe lies $\sim$ 400 keV below the experimental state, indicating that the structure likely involves orbitals outside of the adopted fp model space in the case of the $N = 34$ isotope. The fact that this structure extends to $J \sim 20\hbar$ in ^{60}Fe supports this argument, since the maximum spin available from the $\pi[(f_{7/2})^{-2}] \otimes \nu[(p_{3/2}f_{5/2}p_{1/2})^6]$ configuration is $13\hbar$. Furthermore, the absence of the $J^\pi = 10^+_1 \rightarrow 8^+_1$ γ-ray branch in ^{58}Fe, while a strong transition exists in ^{60}Fe, also suggests a structural difference between these isotopes.

In fact, the extension of the positive-parity sequence above the $J^\pi = 8^+_1$ level in ^{60}Fe appears to be the counterpart of Band 4 in the present work, and that part of the ^{60}Fe positive-parity band is, therefore, labeled

Band 4* hereafter. Figure 7(a) emphasizes the similarity between these two bands, since the data points corresponding to the $J = 10$, 12, 14, and $16\hbar$ levels in Band 4 of ^{58}Fe lie very close to those with the same spins in ^{60}Fe. In this instance, the number of states in the ^{60}Fe band is greater and extends to $J = 20\hbar$, the highest spin populated in the level scheme of Ref. [29].

The two bands shown on the right-hand side of Fig. 5 in Ref. [29], those built on the $J^\pi = 5^-$ and 6^- states at 3516 and 3958 keV, respectively, are possible counterparts of Bands 2 and 3 in ^{58}Fe. These bands in ^{60}Fe are labeled Band 2* and Band 3* hereafter. Not only do the bands begin and end at the same spins in the two isotopes, they also span across similar energy ranges: 12.1 and 11.1 MeV for Bands 2 and 2*, and 9.2 and 8.9 MeV for Bands 3 and 3*, respectively. The two bands in ^{58}Fe do, however, display systematic shifts to higher energies relative to ^{60}Fe, which is likely a direct consequence of the difference in energy of the neutron Fermi surface between the two isotopes. It is also interesting to note that the energies of the two transitions at the top of Band 3 in ^{58}Fe are very similar (2408 and 2412 keV), as are the corresponding transitions of Band 3* in ^{60}Fe (2184 and 2112 keV). These features are highlighted by the turnover in the aligned angular momentum plots for Bands 3 and 3* in Fig. 7(a), although the line for ^{60}Fe begins to turn a little earlier, after the $J = 10\hbar$ state.

The curve for Band 2* in ^{60}Fe exhibits a rather sharp turnover at $J = 15\hbar$, which is a typical characteristic of band termination. However, this feature is not observed for Band 2 in ^{58}Fe. Other differences between Bands 2 and 3 and their counterparts in ^{60}Fe exist, such as the $\Delta J = 1\hbar$ crossover transitions between the unfavored and favored signatures, which are relatively strong in the case of ^{58}Fe and have been observed up to $J = 16\hbar$, while the corresponding γ rays in ^{60}Fe are much weaker and are not seen beyond $J = 10\hbar$.

In other parts of the two level schemes, less well developed structures that may result from similar configurations in the two isotopes are present. One example is the non-yrast band built on the 6740-keV level in ^{60}Fe, which lies in the range $J \sim 9 - 15\hbar$. These could be the corresponding states of those in Band 5 deduced in the present study, but additional information is required to make a more firm statement in this instance.

G. Magnetic rotational bands

The bands labeled MRB 1 and MRB 2 (Magnetic Rotational Bands 1 and 2, respectively) in Fig. 2 are candidates for so-called shears bands and have been investigated in the framework of the self-consistent TAC-RMF model. Some aspects of the theory are given below, although details of similar calculations are provided in Refs. [45, 50].

In the present work, the new parameter set PC-PK1 [52] was used, while pairing correlations were neglected; this issue will be addressed later. The Dirac equation for the nucleons was solved in a three-dimensional Cartesian harmonic-oscillator basis [44, 71] with eight major shells. MRB 1 is assumed to correspond to two aligned proton holes with the configuration $\pi[(f_{7/2})^{-2}] \otimes \nu[(r)^3(g_{9/2})^1]$, where r represents the same shorthand notation used in Section IV A. This configuration is hereafter labeled Config. 1. In this interpretation, the respective spins of the protons and neutrons form the blades of a pair of shears that closes as cranking increases (alignment of the angular momentum vectors), which was discussed in Section I.

In Fig. 9(a), the calculated energy spectra are compared with the available data for MRB 1. The experimental energies are generally reproduced well by the TAC-RMF calculation. However, the assigned configuration could not be followed in the calculations up to the largest observed spin values, since convergent results could not be obtained at $J = 15\hbar$ for Config. 1. By increasing the rotational frequency, it was found that the $\pi[(f_{7/2})^{-3}(r)^1] \otimes \nu[(r)^3(g_{9/2})^1]$ configuration (Config. 2) competes strongly with Config. 1. In fact, the experimental energy levels at higher spin ($J \sim 14 - 15\hbar$) are better reproduced by Config. 2.

Figure 9(b) provides a comparison between the experimental and calculated rotational frequencies as a function of total angular momentum for MRB 1. It is found that the calculated values agree well with the data, which suggests that the present TAC-RMF calculations may also reproduce the moments of inertia well. Around $J = 13\hbar$, the observed band crossing corresponds to a change of configuration. This feature is reproduced by the calculation with Configs. 1 and 2, and emphasizes the difference between the configurations that is not clear from the results presented in Fig. 9(a).

A typical characteristic of magnetic rotation is the presence of strongly enhanced $M1$ transitions at low spin that tend to decrease in strength with increasing angular momentum. In contrast, in-band $E2$ transitions are weak, reflecting the small quadrupole deformation associated with the configurations involved. In Fig. 10(a), calculated $B(M1)$ rates for Configs. 1 and 2 are displayed as a function of spin. Here, the $B(M1)$ values are derived from the relativistic expression of the effective current operator [45], and as in Refs. [44, 50], they are attenuated by a factor of 0.3. It is found that the predicted $B(M1)$ values for Config. 1 exhibit a smooth decreasing tendency, which is characteristic of the shears mechanism. Moreover, the $B(M1)$ values drop suddenly with the change of configuration from Config. 1 to Config. 2 by more than two orders of magnitude.

In Fig. 10(b), calculated $B(E2)$ values are displayed as a function of total angular momentum. For Config. 1, the $B(E2)$ values are very small (< 0.005 e^{2}b^2), in contrast to the large $B(M1)$ values (several μ_N^2). Furthermore, the $B(E2)$ values remain essentially unchanged with increasing angular momentum. However, when the configuration changes to Config. 2, due to the breaking of

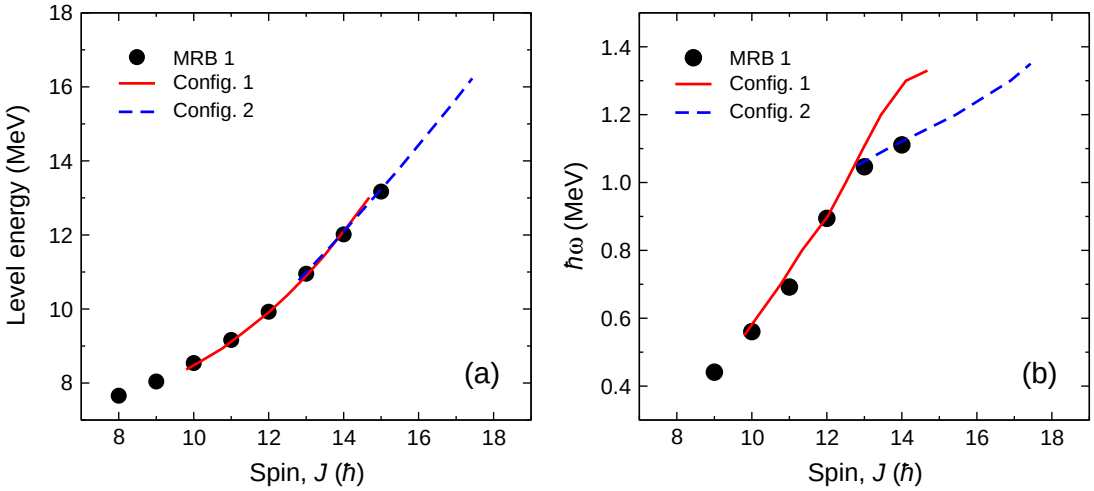

FIG. 9: (Color online) TAC-RMF predictions of (a) level energy and (b) rotational frequency as a function of total angular momentum for the states in MRB 1. The filled black circles represent experimental data, and the energy at $J = 10\hbar$ is taken as a reference value in Panel (a). The self-consistent deformation parameters are $\beta_2 \sim 0.22$, $\gamma \sim 22^\circ - 50^\circ$ for Config. 1 ($\hbar\omega = 0.6 - 1.3$ MeV), and $\beta_2 \sim 0.25$, $\gamma \sim 16^\circ - 4^\circ$ for Config. 2 ($\hbar\omega = 1.0 - 1.3$ MeV).

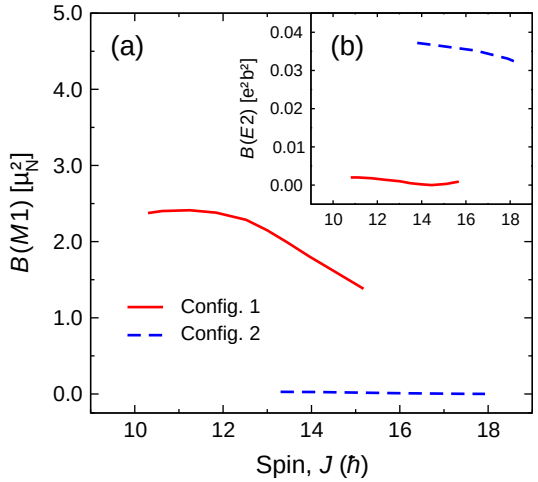

FIG. 10: (Color online) TAC-RMF predictions of (a) $B(M1)$ and (b) $B(E2)$ reduced transition probabilities in MRB 1 as a function of total angular momentum.

an $f_{7/2}$ proton pair, the corresponding $B(E2)$ values are predicted to be $\gtrsim 0.03$ e^{2}b^2, which is of the same order of magnitude as the predicted $B(M1)$ values for Config. 2 in Fig. 10(a).

On the experimental side, a decreasing trend in the $B(M1)/B(E2)$ ratio, which can be deduced from the relative intensities of competing $M1$ and $E2$ in-band γ-ray transitions, is typically adopted as a characteristic of magnetic rotation. However, for the two bands observed in the present study, no $E2$ transitions were observed, and, consequently, such quantities could not be deduced from the data.

Moreover, the parities of MRB 1 and MRB 2 could not be deduced experimentally. However, since the TAC-RMF calculations in Fig. 9 reproduce the experimental results for MRB 1 in a satisfactory manner, an assignment of negative parity seems most likely since the configurations used involve single $\nu g_{9/2}$ excitations. In a similar way to Bands 2 and 3 discussed previously, firm parity assignments for the magnetic rotational bands are desirable.

It should also be noted that the sudden changes of the $B(M1)$ and $B(E2)$ values from Config. 1 to Config. 2, which is similar to the situation in ^{60}Ni, might result from the transition from magnetic rotation in Config. 1 to electric rotation in Config. 2 [50].

As mentioned above, nucleon pairing was omitted from the TAC-RMF calculations. Despite the fact that performing these calculations with pairing is difficult, the adopted approximation might be expected to have an impact on the calculated results. On the one hand, while the significance of pairing in the bands is likely to become somewhat attenuated at the spins populated in MRB 1 ($J \sim 8 - 15\hbar$), the evidence of band crossings in other parts of the level scheme indicates that pairing still plays an important role with respect to the structure of the nucleus, even at high spin. Thus, if pairing effects were included, one might presume that the results of the TAC-RMF model presented in Figs. 9 and 10 would be altered, although the magnitude of such modifications is at present uncertain. On the other hand, the good agreement between the TAC-RMF model and the experimental data suggests that the approximation seems reasonable for the magnetic rotational bands in ^{58}Fe.

It must also be realized that, while the TAC-RMF calculation was able to reproduce MRB 1 in a satisfactory manner, no other particle-hole configuration was found as a plausible counterpart of MRB 2. However, since the two sequences form almost degenerate bands of $\Delta J = 1\hbar$ transitions, the possibility of chiral partner bands [72] cannot be excluded (see, for example, Refs. [73, 74]). De-

tailed investigations in this direction would be interesting, but extend beyond the scope of the present planar cranking calculations. Nevertheless, additional spectroscopic information, such as firm spin-parity assignments and electromagnetic transition probabilities [75], would help to clarify the situation.

Finally, it is noted that similar bands in ^{57}Mn have been observed at $J \sim 13/2 - 21/2\hbar$ above 4-MeV excitation energy, and other candidates for magnetic rotational bands are also present in ^{59}Mn at similar spins starting from $\sim$ 3 MeV [27]. With the recent development of the TAC-RMF model, which satisfactorily reproduces the magnetic structures in ^{58}Fe and ^{60}Ni [50], the candidate bands in the Mn isotopes, although less well developed, might provide further tests of the theory. Moreover, $\Delta J = 1\hbar$ bands at comparable spins and energies to the magnetic rotational bands populated in the present study were previously identified in the even-even neighbor, ^{56}Fe [76]. These bands were interpreted as shell-model states in Ref. [76] rather than shears bands. However, since the $J^\pi = 11^+$ and 12^+ members of the band built on the 8415-keV level in ^{56}Fe lie rather far ($\gtrsim$ 0.5 MeV) from their closest shell-model counterparts (see Figs. 1 and 3 of Ref. [76] for details), an investigation of these $\Delta J = 1\hbar$ bands with the TAC-RMF model is also encouraged.

V. SUMMARY

The structure of ^{58}Fe has been investigated to high spin ($J \sim 17\hbar$) using heavy-ion induced fusion-evaporation reactions at Gammasphere.

Magnetic rotational bands have been observed in this nucleus for the first time: two bands, beginning at $J \sim 8\hbar$, form regular structures composed of low-energy $\Delta J = 1\hbar$ transitions up to $J \sim 15\hbar$. MRB 1 was interpreted within the framework of the TAC-RMF model, which was able to satisfactorily reproduce the experimental results. It is, therefore, concluded that ^{58}Fe is the lightest nucleus so far to exhibit magnetic rotational bands. In the future, lifetime measurements for these states would be useful to test the magnitude and evolution with spin of the $B(M1)$ transition rates predicted by the TAC-RMF model, and to provide an insight into the associated deformation.

In other parts of the ^{58}Fe level scheme, quasirotational structures composed of stretched-$E2$ transitions have been extended to $J \sim 17\hbar$ at an excitation energy $\sim$ 16 MeV, and several other bands are reported for the first time.

The projected shell model (PSM) was applied to investigate these structures at high spin and was generally found to reproduce the bands well with a quadrupole deformation parameter $\epsilon_2 \sim 0.2$ [23]. In the framework of the PSM, Bands 2 and 3 correspond to the favored and unfavored signature partners of a two-quasiparticle (qp) negative-parity band, respectively. These bands involve one qp in a low-Ω Nilsson state of $\nu g_{9/2}$ spherical parentage, and one other qp in the fp shell. Band 4 was interpreted as a 4-qp, $K = 0$ band resulting from a coupling of two 2-qp, $K = 1$ bands: one proton 2-qp configuration involving the $\nu f_{7/2}$ orbital, and one neutron 2-qp configuration of the $\nu g_{9/2}$ orbital. The nature of Band 5 is rather uncertain and may involve configurations that were not considered in Ref. [23]. The ground-state band found adequate description as a 0-qp, $K = 0$ band up to $J^\pi = 12^+$.

Overall, the PSM gives a satisfactory description of the quasirotational bands populated in the present study to high spin, and, notably, it is able to predict with success the regions of band crossings due to the rotational alignments of different qp configurations. These results highlight the importance of the $\nu g_{9/2}$ orbital in the adopted shell-model space.

The parities of most of the high-spin bands identified in the present study are uncertain. While the parities of Bands 2 and 3 are likely negative, and that of Band 4 positive, experimental confirmation is desirable. It is noted that the proposed parities are supported by the PSM calculations.

Numerous positive-parity levels, interpreted here as fp-shell states, were also deduced in the present study. These provided thorough tests of the spherical shell model, where three different effective interactions were generally able to reproduce the low-lying data in a satisfactory manner, but were found to deviate from the experimental results at higher energy and spin. Such deviations are likely to be the consequence of using a restrictive fp model space. Overall, it is nevertheless concluded that the GXPF1A Hamiltonian is generally the more successful of the interactions tested here, at least over the subset of states populated.

The results of the present study clearly illustrate the importance of orbitals outside the fp model space for a proper understanding of nuclei in this mass region. Indeed, while current large-scale shell-model calculations do rather well for reproducing positive-parity states at low spin and excitation energy in even-even systems, the expansion of the fp model space with the inclusion of the $\nu g_{9/2}$ orbital and other states from higher shells presents a challenge. It has been shown that adroit truncations in the adopted model space, such as that presented by the use of Nilsson orbitals in the PSM, can make headway in the understanding of near-yrast states. However, the development of robust interactions for shell models encompassing full $fpg_{9/2}$ spaces is an ever growing priority to properly describe medium-mass nuclei. This is true even in the case of ^{58}Fe, which lies along the valley of stability.

Acknowledgments

The authors thank Prof. M. Freer at the University of Birmingham for the loan of the ^{14}C target. This work was

supported by the UK Science and Technology Facilities Council (STFC), the US Department of Energy, Office of Nuclear Physics, under contract numbers DE-AC02-06CH11357 and DE-FG02-94ER40848, the US National Science Foundation under grant PHY-0139950, and the Natural Science Foundation of China under grant numbers 10975007, 10975008, 11005069, 11075103, 11135005, and 11175002.

[1] J. I. Prisciandaro, P. F. Mantica, B. A. Brown, D. W. Anthony, M. W. Cooper, A. Garcia, D. E. Groh, A. Komives, W. Kumarasiri, P. A. Lofy, *et al.*, Phys. Lett. B **510**, 17 (2001).
[2] D. E. Appelbe, C. J. Barton, M. H. Muikku, J. Simpson, D. D. Warner, C. W. Beausang, M. A. Caprio, J. R. Cooper, J. R. Novak, N. V. Zamfir, *et al.*, Phys. Rev. C **67**, 034309 (2003).
[3] A. Bürger, T. R. Saito, H. Grawe, H. Hübei, P. Reiter, J. Gerl, M. Górska, H. J. Wollersheim, A. Al-Khatib, A. Banu, *et al.*, Phys. Lett. B **622**, 29 (2005).
[4] C. Guénaut, G. Audi, D. Beck, K. Blaum, G. Bollen, P. Delahaye, F. Herfurth, A. Kellerbauer, H.-J. Kluge, D. Lunney, *et al.*, J. Phys. G: Nucl. Part. Phys. **31**, S1765 (2005).
[5] R. V. F. Janssens, B. Fornal, P. F. Mantica, B. A. Brown, R. Broda, P. Bhattacharyya, M. P. Carpenter, M. Cinausero, P. J. Daly, A. D. Davies, *et al.*, Phys. Lett. B **546**, 55 (2002).
[6] D.-C. Dinca, R. V. F. Janssens, A. Gade, D. Bazin, R. Broda, B. A. Brown, C. M. Campbell, M. P. Carpenter, P. Chowdhury, J. M. Cook, *et al.*, Phys. Rev. C **71**, 041302(R) (2005).
[7] A. Huck, G. Klotz, A. Knipper, C. Miehé, C. Richard-Serre, G. Walter, A. Poves, H. L. Ravn, and G. Marguier, Phys. Rev. C **31**, 2226 (1985).
[8] A. Gade, R. V. F. Janssens, D. Bazin, R. Broda, B. A. Brown, C. M. Campbell, M. P. Carpenter, J. M. Cook, A. N. Deacon, D.-C. Dinca, *et al.*, Phys. Rev. C **74**, 021302(R) (2006).
[9] Takaharu Otsuka, Toshio Suzuki, Rintaro Fujimoto, Hubert Grawe, and Yoshinori Akaishi, Phys. Rev. Lett. **95**, 232502 (2005).
[10] M. Honma, T. Otsuka, B. A. Brown, and T. Mizusaki, Phys. Rev. C **65**, 061301(R) (2002).
[11] S. N. Liddick, P. F. Mantica, R. V. F. Janssens, R. Broda, B. A. Brown, M. P. Carpenter, B. Fornal, M. Honma, T. Mizusaki, A. C. Morton, *et al.*, Phys. Rev. Lett. **92**, 072502 (2004).
[12] M. Honma, T. Otsuka, B. A. Brown, and T. Mizusaki, Eur. Phys. J. A **25**, s01, 499 (2005).
[13] A. Poves, J. Sánchez-Solano, E. Caurier, and F. Nowacki, Nucl. Phys. A **694**, 157 (2001).
[14] W. A. Richter, M. G. van der Merwe, R. E. Julies, and B. A. Brown, Nucl. Phys. A **523**, 325 (1991).
[15] S. J. Freeman, R. V. F. Janssens, B. A. Brown, M. P. Carpenter, S. M. Fischer, N. J. Hammond, M. Honma, T. Lauritsen, C. J. Lister, T. L. Khoo, *et al.*, Phys. Rev. C **69**, 064301 (2004).
[16] S. Zhu, A. N. Deacon, S. J. Freeman, R. V. F. Janssens, B. Fornal, M. Honma, F. R. Xu, R. Broda, I. R. Calderin, M. P. Carpenter, *et al.*, Phys. Rev. C **74**, 064315 (2006).
[17] N. Aoi, E. Takeshita, H. Suzuki, S. Takeuchi, S. Ota, H. Baba, S. Bishop, T. Fukui, Y. Hashimoto, H. J. Ong, *et al.*, Phys. Rev. Lett. **102**, 012502 (2009).
[18] A. Gade, R. V. F. Janssens, T. Baugher, D. Bazin, B. A. Brown, M. P. Carpenter, C. J. Chiara, A. N. Deacon, S. J. Freeman, G. F. Grinyer, *et al.*, Phys. Rev. C **81**, 051304(R) (2010).
[19] P. Adrich, A. M. Amthor, D. Bazin, M. D. Bowen, B. A. Brown, C. M. Campbell, J. M. Cook, A. Gade, D. Galaviz, T. Glasmacher, *et al.*, Phys. Rev. C **77**, 054306 (2008).
[20] S. M. Lenzi, F. Nowacki, A. Poves, and K. Sieja, Phys. Rev. C **82**, 054301 (2010).
[21] E. Caurier, F. Nowacki, and A. Poves, Eur. Phys. J. A **15**, 145 (2002).
[22] Kenji Hara and Yang Sun, Int. J. Mod. Phys. E **4**, 637 (1995).
[23] Yang Sun, Ying-Chun Yang, Hong-Liang Liu, Kazunari Kaneko, Munetake Hasegawa, and Takahiro Mizusaki, Phys. Rev. C **80**, 054306 (2009).
[24] Yingchun Yang, Yang Sun, Kazunari Kaneko, and Munetake Hasegawa, Phys. Rev. C **82**, 031304(R) (2010).
[25] Ying-Chun Yang, Hua Jin, Yang Sun, and Kazunari Kaneko, Phys. Lett. B **700**, 44 (2011).
[26] A. N. Deacon, S. J. Freeman, R. V. F. Janssens, F. R. Xu, M. P. Carpenter, I. R. Calderin, P. Chowdhury, N. J. Hammond, T. Lauritsen, C. J. Lister, *et al.*, Phys. Lett. B **622**, 151 (2005).
[27] D. Steppenbeck, A. N. Deacon, S. J. Freeman, R. V. F. Janssens, S. Zhu, M. P. Carpenter, P. Chowdhury, M. Honma, T. Lauritsen, C. J. Lister, *et al.*, Phys. Rev. C **81**, 014305 (2010).
[28] C. J. Chiara, I. Stefanescu, N. Hoteling, W. B. Walters, R. V. F. Janssens, R. Broda, M. P. Carpenter, B. Fornal, A. A. Hecht, W. Królas, *et al.*, Phys. Rev. C **82**, 054313 (2010).
[29] A. N. Deacon, S. J. Freeman, R. V. F. Janssens, M. Honma, M. P. Carpenter, P. Chowdhury, T. Lauritsen, C. J. Lister, D. Seweryniak, J. F. Smith, *et al.*, Phys. Rev. C **76**, 054303 (2007).
[30] N. Hoteling, C. J. Chiara, R. Broda, W. B. Walters, R. V. F. Janssens, M. Hjorth-Jensen, M. P. Carpenter, B. Fornal, A. A. Hecht, W. Królas, *et al.*, Phys. Rev. C **82**, 044305 (2010).
[31] A. N. Deacon, D. Steppenbeck, S. Zhu, S. J. Freeman, R. V. F. Janssens, M. P. Carpenter, B. Fornal, M. Honma, B. P. Kay, F. G. Kondev, *et al.*, Phys. Rev. C **83**, 064305 (2011).
[32] R. M. Clark and A. O. Macchiavelli, Ann. Rev. Nucl. Part. Sci. **50**, 1 (2000).
[33] S. Frauendorf, Rev. Mod. Phys. **73**, 463 (2001).
[34] H. Hübel, Prog. Part. Nucl. Phys. **54**, 1 (2005).
[35] S. Frauendorf, Nucl. Phys. A **557**, 259c (1993).
[36] S. Frauendorf, J. Meng, and J. Reif, *Proceedings of the Conference on Physics From Large γ-Ray Detector Arrays*, edited by M. A. Deleplanque (Univ. of California, Berkeley, 1994), vol. II of Report LBL35687, p. 52.
[37] R. M. Clark, R. Wadsworth, E. S. Paul, C. W. Beausang,

I. Ali, A. Astier, D. M. Cullen, P. J. Dagnall, P. Fallon, M. J. Joyce, *et al.*, Phys. Lett. B **275**, 247 (1992).
[38] G. Baldsiefen, H. Hübel, D. Mehta, B. V. T. Rao, U. Birkental, G. Fröhlingsdorf, M. Neffgen, N. Nenoff, S. C. Pancholi, N. Singh, *et al.*, Phys. Lett. B **275**, 252 (1992).
[39] A. Kuhnert, M. A. Stoyer, J. A. Becker, E. A. Henry, M. J. Brinkman, S. W. Yates, T. F. Wang, J. A. Cizewski, F. S. Stephens, M. A. Deleplanque, *et al.*, Phys. Rev. C **46**, 133 (1992).
[40] R. M. Clark, S. J. Asztalos, G. Baldsiefen, J. A. Becker, L. Bernstein, M. A. Deleplanque, R. M. Diamond, P. Fallon, I. M. Hibbert, H. Hübel, *et al.*, Phys. Rev. Lett. **78**, 1868 (1997).
[41] Amita, Ashok Kumar Jain, and Balraj Singh, At. Data and Nucl. Data Tables **74**, 283 (2000), revised edition available online from Ref. [58].
[42] D. A. Torres, F. Cristancho, L.-L. Andersson, E. K. Johansson, D. Rudolph, C. Fahlander, J. Ekman, R. du Rietz, C. Andreoiu, M. P. Carpenter, *et al.*, Phys. Rev. C **78**, 054318 (2008).
[43] Stefan Frauendorf and Jie Meng, Z. Phys. A **356**, 263 (1996).
[44] H. Madokoro, J. Meng, M. Matsuzaki, and S. Yamaji, Phys. Rev. C **62**, 061301 (2000).
[45] J. Peng, J. Meng, P. Ring, and S. Q. Zhang, Phys. Rev. C **78**, 024313 (2008).
[46] P. Olbratowski, J. Dobaczewski, J. Dudek, T. Rzaca-Urban, Z. Marcinkowska, and R. M. Lieder, Acta Phys. Pol. B **33**, 389 (2002).
[47] P. Olbratowski, J. Dobaczewski, J. Dudek, and W. Plóciennik, Phys. Rev. Lett. **93**, 052501 (2004).
[48] P. Ring, Prog. Part. Nucl. Phys. **37**, 193 (1996).
[49] J. Meng, H. Toki, S. Zhou, S. Zhang, W. Long, and L. Geng, Prog. Part. Nucl. Phys. **57**, 470 (2006).
[50] P. W. Zhao, S. Q. Zhang, J. Peng, H. Z. Liang, P. Ring, and J. Meng, Phys. Lett. B **699**, 181 (2011).
[51] L. F. Yu, P. W. Zhao, S. Q. Zhang, P. Ring, and J. Meng, Phys. Rev. C **85**, 024318 (2012).
[52] P. W. Zhao, Z. P. Li, J. M. Yao, and J. Meng, Phys. Rev. C **82**, 054319 (2010).
[53] P. W. Zhao, J. Peng, H. Z. Liang, P. Ring, and J. Meng, Phys. Rev. Lett. **107**, 122501 (2011).
[54] I. Y. Lee, Nucl. Phys. A **520**, 641c (1990).
[55] Lowell M. Bollinger, Ann. Rev. Nucl. Part. Sci. **36**, 475 (1986).
[56] L. M. Bollinger, R. C. Pardo, K. W. Shepard, J. M. Bogaty, B. E. Clifft, F. H. Munson, and G. Zinkann, Nucl. Instrum. and Meth. A **328**, 221 (1993).
[57] Caroline D. Nesaraja, Scott D. Geraedts, and Balraj Singh, Nucl. Data Sheets **111**, 897 (2010), and references therein.
[58] URL `http://www.nndc.bnl.gov/ensdf/`.
[59] R. M. Diamond, E. Matthias, J. O. Newton, and F. S. Stephens, Phys. Rev. Lett. **16**, 1205 (1966).
[60] T. Yamazaki, Nucl. Data A **3**, 1 (1967), and references therein.
[61] A. Krämer-Flecken, T. Morek, R. M. Lieder, W. Gast, G. Hebbinghaus, H. M. Jäger, and W. Urban, Nucl. Instrum. and Meth. A **275**, 333 (1989).
[62] A. M. Nathan, J. W. Olness, E. K. Warburton, and J. B. McGrory, Phys. Rev. C **17**, 1008 (1978).
[63] S. Cavallaro, J. Delaunay, R. Ballini, T. Nomura, N. Bendjaballah, and C. Tosello, Nucl. Phys. A **293**, 125 (1977).
[64] G. S. Mani, Nucl. Phys. A **169**, 194 (1971).
[65] H. H. Bolotin, A. E. Stuchbery, K. Amos, and I. Morrison, Nucl. Phys. A **311**, 75 (1978).
[66] C. Chasman, K. W. Jones, and R. A. Ristinen, Nucl. Instrum. and Meth. **37**, 1 (1965).
[67] W. D. M. Rae, NuShellX for Windows and Linux, unpublished.
[68] T. Mizusaki, N. Shimizu, Y. Utsuno, and M. Honma, MSHELL64, unpublished.
[69] K. Kaneko, Y. Sun, M. Hasegawa, and T. Mizusaki, Phys. Rev. C **78**, 064312 (2008).
[70] Sven Gösta Nilsson, Chin Fu Tsang, Adam Sobiczewski, Zdzislaw Szymański, Slawomir Wycech, Christer Gustafson, Inger-Lena Lamm, Peter Möller, and Björn Nilsson, Nucl. Phys. A **131**, 1 (1969).
[71] W. Koepf and P. Ring, Nucl. Phys. A **493**, 61 (1989).
[72] S. Frauendorf and Jie Meng, Nucl. Phys. A **617**, 131 (1997).
[73] K. Starosta, T. Koike, C. J. Chiara, D. B. Fossan, D. R. LaFosse, A. A. Hecht, C. W. Beausang, M. A. Caprio, J. R. Cooper, R. Krücken, *et al.*, Phys. Rev. Lett. **86**, 971 (2001).
[74] C. Vaman, D. B. Fossan, T. Koike, K. Starosta, I. Y. Lee, and A. O. Macchiavelli, Phys. Rev. Lett. **92**, 032501 (2004).
[75] T. Koike, K. Starosta, and I. Hamamoto, Phys. Rev. Lett. **93**, 172502 (2004).
[76] D. E. Appelbe, G. Martínez-Pinedo, R. A. E. Austin, J. A. Cameron, J. Chenkin, T. E. Drake, B. Djerroud, S. Flibotte, D. N. Parker, C. E. Svensson, *et al.*, Phys. Rev. C **62**, 064314 (2000).